Icarus 223 (2013) 654–676

Contents lists available at SciVerse ScienceDirect

Icarus

journal homepage: www.elsevier.com/locate/icarus

Zonal wavenumber three traveling waves in the northern hemisphere of Mars simulated with a general circulation model

Huiqun Wang [a,*], Mark I. Richardson [b], Anthony D. Toigo [c], Claire E. Newman [b]

[a] Harvard-Smithsonian Center for Astrophysics, Cambridge, MA 02138, USA
[b] Ashima Research, Pasadena, CA 91101, USA
[c] Applied Physics Laboratory, Johns Hopkins University, Laurel, MD 20723, USA

ARTICLE INFO

Article history:
Received 23 January 2012
Revised 8 January 2013
Accepted 8 January 2013
Available online 4 February 2013

Keywords:
Atmospheres, Dynamics
Mars
Mars, Atmosphere

ABSTRACT

Observations suggest a strong correlation between curvilinear shaped traveling dust storms (observed in wide angle camera images) and eastward traveling zonal wave number $m = 3$ waves (observed in thermal data) in the northern mid and high latitudes during the fall and winter. Using the MarsWRF General Circulation Model, we have investigated the seasonality, structure and dynamics of the simulated $m = 3$ traveling waves and tested the hypothesis that traveling dust storms may enhance $m = 3$ traveling waves under certain conditions.

Our standard simulation using a prescribed "MGS dust scenario" can capture the observed major wave modes and strong near surface temperature variations before and after the northern winter solstice. The same seasonal pattern is also shown by the simulated near surface meridional wind, but not by the normalized surface pressure. The simulated eastward traveling $1.4 < T < 10$ sol $m = 3$ waves are confined near the surface in terms of the temperature perturbation, EP flux and eddy available potential energy, and they extend higher in terms of the eddy winds and eddy kinetic energy. The signature of the simulated $m = 3$ traveling waves is stronger in the near surface meridional wind than in the near surface temperature field.

Compared with the standard simulation, our test simulations show that the prescribed $m = 3$ traveling dust blobs can enhance the simulated $m = 3$ traveling waves during the pre- and post-solstice periods when traveling dust storms are frequently observed in images, and that they have negligible effect during the northern winter solstice period when traveling dust storms are absent. The enhancement is even greater in our simulation when dust is concentrated closer to the surface. Our simulations also suggest that dust within the 45–75°N band is most effective at enhancing the simulated $m = 3$ traveling waves.

There are multiple factors influencing the strength of the simulated $m = 3$ traveling waves. Among those, our study suggests that weaker near surface static stability, larger near surface baroclinic parameter, and wave-form dust forcing for latitudinally extended dust storms are favorable. Further study is needed to fully understand the importance of these factors and others.

© 2013 Elsevier Inc. All rights reserved.

1. Introduction

Traveling waves are prominent in the martian atmosphere. Using the Mars Global Surveyor (MGS) Thermal Emission Spectrometer (TES) temperature data, Banfield et al. (2004) found strong zonal wave number $m = 1$, 2 and 3 traveling waves in the vicinity of the polar jet, with maximum amplitudes attained above 25 km for the $m = 1$ waves and near the surface for the $m = 3$ waves. They also found that the typical wave periods were $T = 2.5$–30 sols for the $m = 1$ waves, $T = 2$–10 sols for the $m = 2$ waves and $T = 2$–3 sols for the $m = 3$ waves. These results were consistent with the results derived from the Viking data (Barnes, 1980). Previous studies using various Mars General Circulation Models (GCMs) reproduced many general characteristics of the traveling waves (Barnes et al., 1993; Basu et al., 2006; Collins et al., 2006; Wilson et al., 2006). In this paper, we use the MarsWRF GCM and focus on the structure and behavior of the eastward traveling zonal wavenumber $m = 3$ waves, as the observations suggest a strong correlation between these waves derived from the temperature data and the curvilinear shaped dust storms shown in images in the northern hemisphere during the fall and winter (Wang et al., 2005; Wang, 2007; Hinson and Wang, 2010; Hinson et al., 2012). In addition, we test whether it is possible for traveling dust storms to enhance $m = 3$ traveling waves in our simulations.

Curvilinear dust storms are analogous in morphology to terrestrial baroclinic storms and are commonly observed in the mid/high

* Corresponding author.
E-mail address: hwang@cfa.harvard.edu (H. Wang).

0019-1035/$ - see front matter © 2013 Elsevier Inc. All rights reserved.
http://dx.doi.org/10.1016/j.icarus.2013.01.004

latitudes on Mars. Fig. 1 shows a sequence of curvilinear dust storms (labeled by their arbitrarily assigned event numbers) observed by the MGS Mars Observer Camera (MOC) on six consecutive sols in mid northern fall of Mars year 27 (2004–2005). Each image is a reprojection of an "equatorial" Mars Daily Global Map (MDGM, 60°S–60°N) (Wang and Ingersoll, 2002) from simple cylindrical projection to polar stereographic projection (0–90°N). These dust storms generally travel eastward and some can be tracked for several sols. Curvilinear dust storms are important in the martian dust cycle. They can sometimes develop into flushing dust storms that transport dust southward from the northern high latitudes to the low latitudes (e.g., Event 1, 5 and 7 in Fig. 1), and may even lead to major planet-encircling dust storm that greatly affects the global circulation (Wang et al., 2003; Basu et al., 2006).

Fig. 2 shows the close correspondence between the incidences of the curvilinear dust storms in MOC images and the amplitudes of the zonal wavenumber $m = 3$ traveling waves derived from TES temperature data for Mars year 24 (left) and 26 (right) (Mars year 25 is not shown because of the influence of the 2001 global dust storm [e.g. Strausberg et al., 2005; Cantor, 2007]). The TES temperature data are from the PDS Geosciences Node (http://geo.pds.nasa.gov, see Conrath et al. (2000) for retrieval algorithm). The standard deviation of the 2 PM TES temperature at 610 Pa is shown in the top row of Fig. 2. It is calculated for each 2° latitude × 30° longitude × 15° Ls bin, and then zonally averaged. The result for the 475 Pa level is similar (Wang et al., 2005; Wang, 2007). The strong near surface temperature variations indicative of strong eddies before and after the northern winter solstice period (Ls = 240–300°) appear to coincide with the occurrences of curvilinear dust storms (symbols in the bottom panels).

To examine the contributions of various waves, we decompose the temperature anomalies (with respect to the 30-sol running

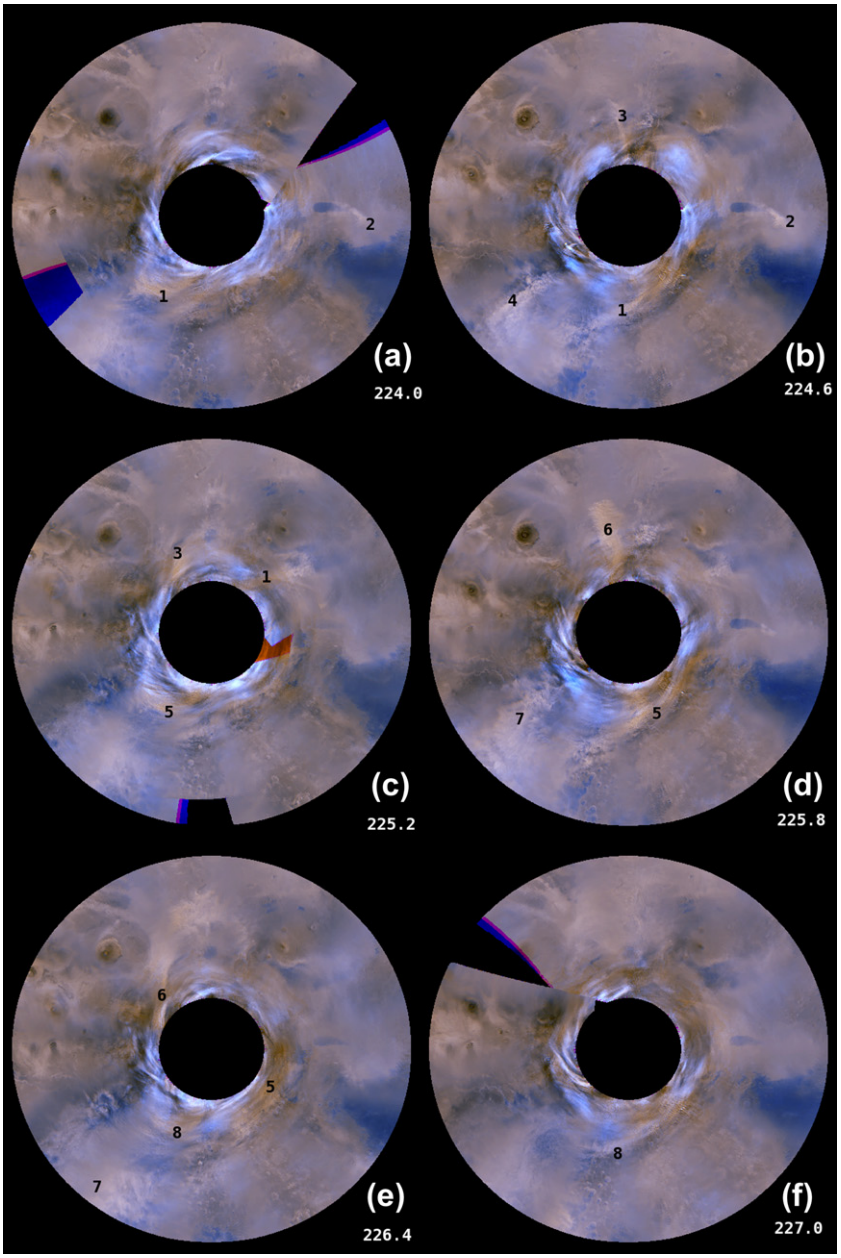

Fig. 1. Polar stereographically projected (0–90°N) MGS MOC Mars Daily Global Maps (60°S–60°N, 0.1° × 0.1°) for 6 consecutive sols during Ls = 224.0–227.0° in Mars year 27. The numbers in the images label the curvilinear shaped dust storms or dust storms that are related to them. Some dust storms can be tracked for several sols.

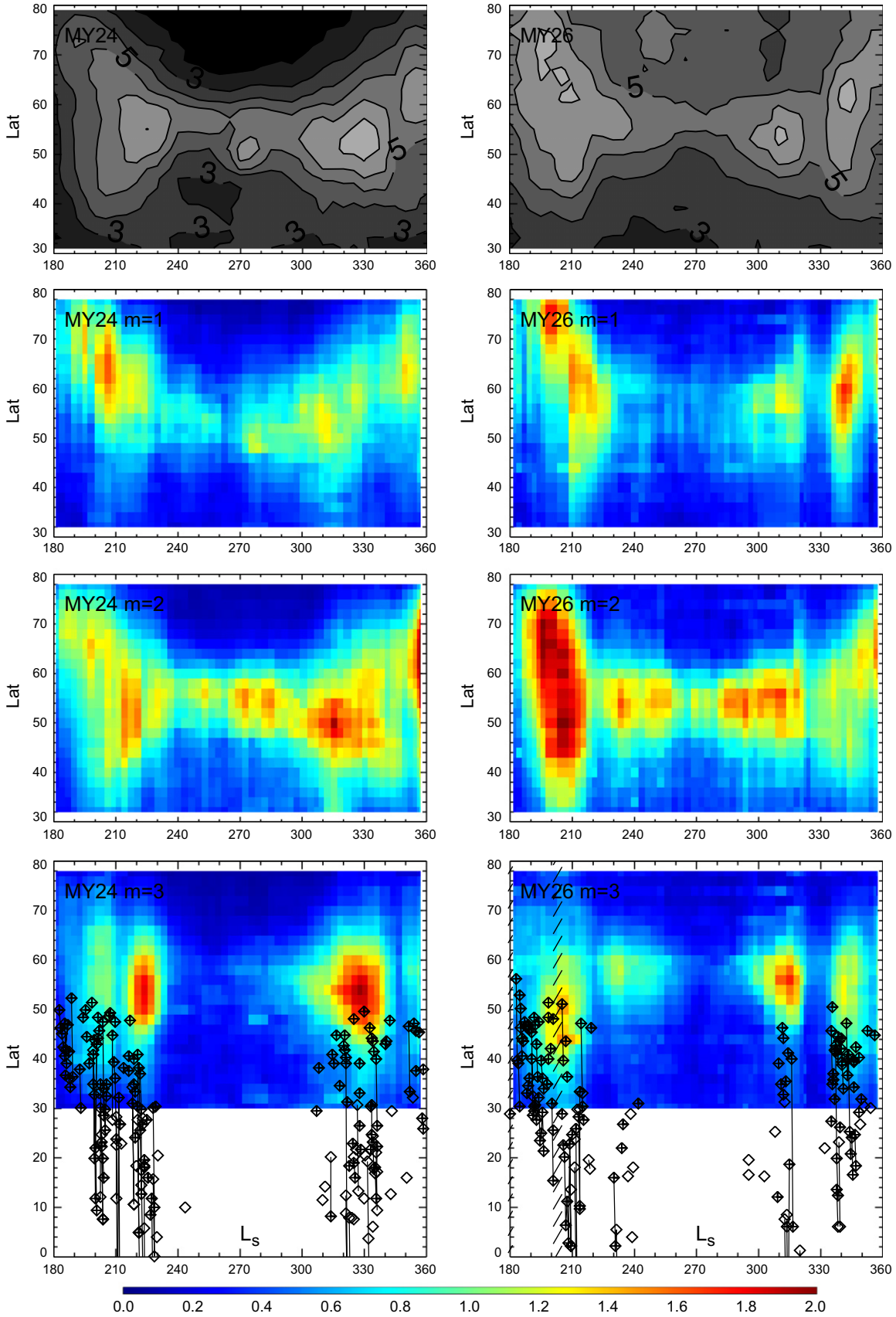

Fig. 2. (Top row) The standard deviation (K) of the 2 PM MGS TES temperature at 610 Pa as a function of Ls and latitude. (Rows 2–4) The mean amplitude (K) of the eastward traveling waves whose wave periods are $1.4 < T < 10.0$ sol for zonal wave number $m = 1$, 2 and 3 waves as a function of Ls and latitude. The incidences of the curvilinear dust storms and their related events observed in MOC images are superimposed on the bottom panels. The latitudes of the symbols correspond to the southern tips of the dust storms. Diamonds with plus signs denote curvilinear shaped dust storms. Open diamonds denote dust storms that can be traced back to curvilinear dust storms or ambiguous cases. The events that last for multiple sols are linked with lines. The panels in the left column are for Mars year 24 and those in the right column are for Mars year 26.

mean for each 2° latitudinal band) at 610 Pa into different wave modes by calculating the periodogram for zonal wave number $m = 1$, 2 and 3 waves using the least squares method described in Wu et al. (1995). The mean amplitudes of the eastward traveling $m = 1$, 2 and 3 waves whose wave periods (T) are between 1.4 and 10.0 sols are shown in the bottom three rows of Fig. 2. These plots are spectrally averaged. Individual wave mode within the spectral band can have larger or smaller amplitudes. For easy comparison, we have over-plotted on the $m = 3$ panels the Ls values and southern tip latitudes of the events that are related to curvilinear dust storms observed by MGS MOC (Wang, 2007). These events include both curvilinear shaped dust storms themselves (diamonds with plus signs) and amorphous dust storms (diamonds) that can be traced back to curvilinear shaped dust storms or ambiguous cases (diamonds).

All three wave numbers show generally wider latitudinal influence before and after the northern winter solstice period. However, the seasonal variation of the wave amplitude depends on the latitude. For example, in Mars year 24, the $m = 2$ waves have similar amplitudes during Ls = 270–300° as those during Ls = 210–240° at 56°N, but have greatly reduced amplitudes during Ls = 240–300° at 46°N and 64°N. The $m = 1$ and $m = 2$ waves can be strong north of 60°N near the fall and spring equinoxes, in addition to their presence south of 60°N during other time periods, but the $m = 3$ waves only show significant amplitudes (>1 K) south of about 60°N during Ls = 200–240° and Ls = 300–350°. Sometimes, the $m = 3$ waves are accompanied by strong $m = 1$ or $m = 2$ waves. During Ls = 200–210° in Mars year 26, the $m = 2$ waves are actually stronger than the $m = 3$ waves. Nevertheless, the $m = 3$ waves are clearly present as well. In summary, Fig. 2 shows a nice correlation between the traveling dust storms and the $m = 3$ traveling waves, suggesting a link between them.

The potential importance of the $m = 3$ traveling waves in the martian dust cycle leads us to do a detailed investigation of the structure and behavior of these waves using the MarsWRF GCM. Moreover, we test the hypothesis that traveling dust storms may enhance the strength of $m = 3$ traveling waves in the atmosphere, providing a potential positive feedback where the dust storms associated with the $m = 3$ traveling waves lead to more dust lifting and stronger $m = 3$ traveling waves. Idealized dust forcing is used in our simulations to make the connection between the forcing and response as direct and traceable as possible.

As will be shown in Section 3, our standard simulation using the Mars Climate Database (Lewis et al., 1999) "MGS dust scenario" (described in detail in Montmessin et al. (2004)) can reproduce the general seasonality and wave modes of the observed transient eddies, but the simulated $m = 3$ traveling waves appear relatively weak compared to the observation. In Section 4, we will show that additional prescribed traveling dust storms can enhance the simulated $m = 3$ traveling waves with respect to those in the standard simulation.

The deficiency of the $m = 3$ traveling waves in the standard simulation presented in this paper should not be considered as a general problem of the MarsWRF model. Since the martian circulation is highly sensitive to dust distribution (e.g., Barnes et al., 1993; Wilson et al., 2002), strong $m = 3$ traveling waves can probably be generated by MarsWRF with other prescribed dust scenarios. Different choices of model physics and computational grid may influence the simulation results as well. Using the LMD/Oxford Mars GCMs, Collins et al. (1996) found dominant zonal wave number 1 and 2 traveling waves. Previous studies with the NASA Ames and GFDL Mars GCMs found strong $m = 3$ traveling waves (Barnes et al., 1993; Basu et al., 2006; Wang et al., 2003; Wilson et al., 2006). Here, we simply use the standard MarsWRF simulation as a baseline for comparison in order to test the effect of the prescribed traveling dust storms under the "MGS dust scenario" background. Our numerical experiments suggest that, at least under certain circumstances we examined (Section 4), the $m = 3$ traveling dust storms can enhance the $m = 3$ traveling waves, leading to a potential positive feedback.

The simulations in this study do not include clouds. It should be noted that previous studies found that clouds could significantly influence atmospheric thermal structure and circulation (Hinson and Wilson, 2004; Wilson et al., 2007, 2008). In particular, recent GCM studies by Wilson et al. (2011) and Kahre et al. (2012) suggest that clouds could enhance transient eddies near the polar cap edge which could in turn affect dust lifting. We acknowledge the importance of clouds, but in this paper, we focus on a different aspect – the effect of dust itself on the simulated $m = 3$ traveling waves, and we pay special attention to a specific zonal wave number $m = 3$.

2. Model description

The MarsWRF model is the Mars version of PlanetWRF, a general purpose, local to global numerical model for planetary atmospheres (Richardson et al., 2007). PlanetWRF is a grid point model using the Arakawa C-grid and a terrain-following σ coordinate. The simulations in this study use the version of MarsWRF described in Toigo et al. (2012) and have 5° latitude × 5° longitude horizontal resolution with 40 vertical layers between the surface and 0.006 Pa. The surface topography, albedo, thermal inertia, emissivity, roughness, and terrain slope are based on MGS observations. A 'sponge layer' is used near the top of the domain to prevent spurious eddy reflections from the model top. The model radiative transfer scheme for CO_2 and dust is based on Hourdin (1992) (CO_2 in the thermal infrared), Haberle et al. (1982) (dust in the infrared), Briegleb (1992) (dust in the visible) and Forget et al. (1999) (CO_2 in the infrared), and includes non-LTE cooling above 60 km based on tabulated cooling rates (López-Valverde and López-Puertas, 1994). Dust has a single scattering albedo of 0.92 and an asymmetry factor of 0.55. The visible-to-IR ratio is tuned to be 1.0:0.7 so that the modeled temperature field best matches the MGS TES observation (Richardson et al., 2007). The model includes a simple CO_2 condensation and sublimation scheme that successfully reproduces the Viking Lander surface pressure cycle (Guo et al., 2009). The PBL parameterization uses the Yonsei University (YSU) non-local mixing scheme (Hong et al., 2006). The surface layer scheme uses stability functions from Paulson (1970), Dyer and Hicks (1970), and Webb (1970) to compute surface exchange coefficients. Thermal diffusion within the subsurface is represented by a 15-layer implicit solver. The version used for this paper does not include an active water cycle or dynamically interactive dust.

In this study, the model dust is prescribed as a space and time varying function. Specifically, we use the Mars Climate Database "MGS dust scenario" as our "standard" dust distribution. This scenario was developed as an attempt to broadly reproduce the MGS observations of temperature (which is strongly dependent on dust) in the first MGS mapping year. The spikes due to major dust storms were removed. So, it attempts to represent a typical storm-free year on Mars. Fig. 3a shows the zonally averaged cumulative dust optical depth at the surface as a function of Ls and latitude for the standard simulation. The maximum optical depth ($\tau \approx 0.5$) occurs between 20°N and 30°N at perihelion (Ls = 251°). A small amount of dust ($\tau < 0.2$) is present over the planet during northern spring and summer and at the northern high latitudes (>60°N) throughout the year.

The vertical profile of the cumulative dust optical depth is shown by the solid black line in Fig. 4. It is similar to the form described by Conrath (1975). Dust is approximately uniformly mixed in the lower atmosphere and decreases to a "dust top" altitude,

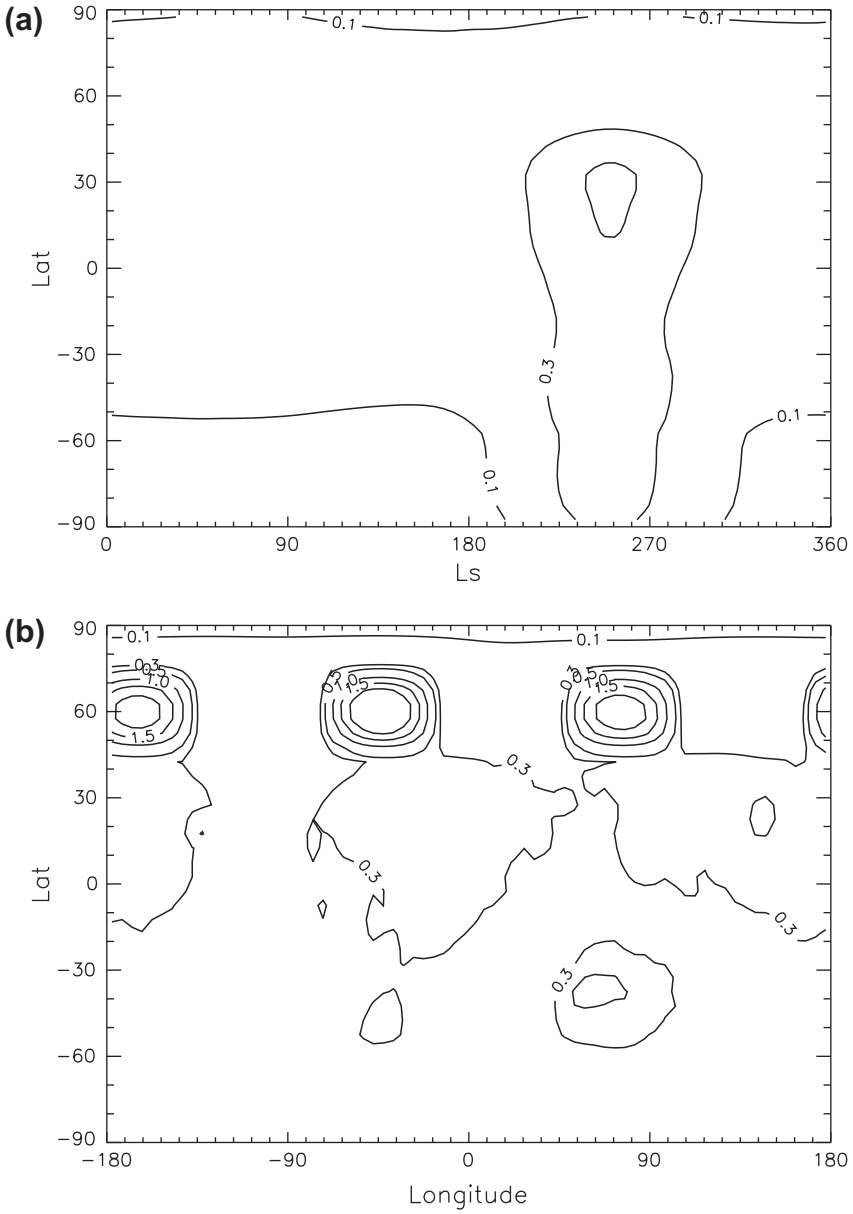

Fig. 3. (a) The zonally averaged cumulative dust optical depth at the surface as a function of Ls and latitude for the standard simulation. (b) A snapshot of the longitude versus latitude distribution of cumulative dust optical depth at the surface at Ls = 216° in Test 1.

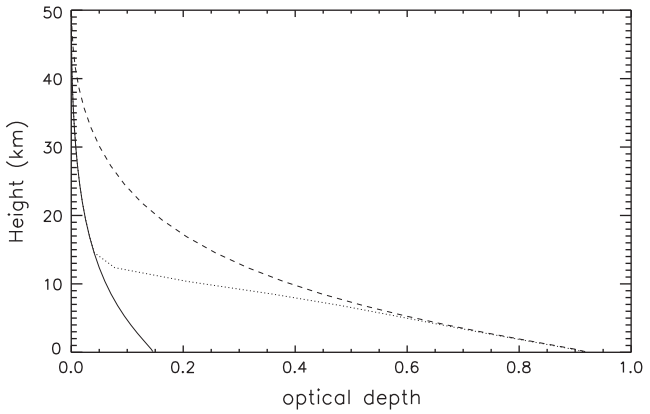

Fig. 4. The zonal mean vertical profile of the cumulative dust optical depth at 57.5°N and Ls = 217.5° for (solid line) the standard simulation, (dashed line) Test 1 and Test 2, and (dotted line) Test 3. Only the lowest 50 km is plotted.

where it rapidly drops to zero. The "dust top" altitude is a function of latitude and Ls (Montmessin et al., 2004).

We have also performed simulations with additional idealized dust in the northern mid to high latitudes during Ls = 180–360° (Fig. 3b) in order to test the response of the $m = 3$ traveling waves. These experiments are motivated by the numerous curvilinear dust storms in MOC images (Fig. 1 and 2) that are not included in the "MGS dust scenario" (Fig. 3a). Smith (2008) summarized the dust optical depth distribution observed by MGS TES. However, due to the difficulty of retrieval over cold surfaces, nadir data within and around the cold polar vortex are usually missing. Curvilinear dust storms mainly reside in the vicinity of the cold polar vortex where reliable TES retrievals are lacking. As an example, Fig. 5 shows four MDGMs (60°S–60°N) during Ls = 202–210° of Mars year 24 with the corresponding TES dust optical depths superimposed. TES captures some curvilinear dust storms, especially when the dust storms have moved south. However, it only samples the southern tips of most mid/high latitude events, missing the most

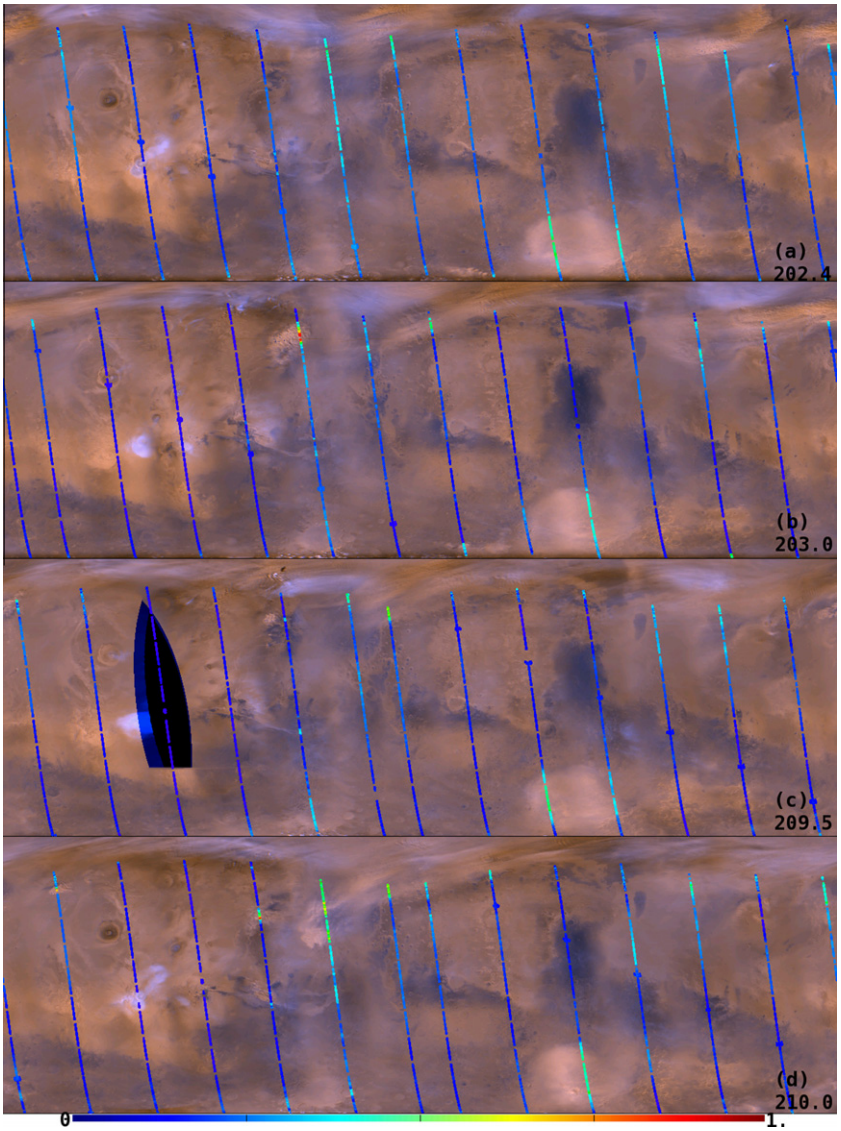

Fig. 5. MGS MOC Mars Daily Global Maps (60°S–60°N, 0.1° × 0.1°) for (a) Ls = 202.4°, (b) Ls = 203.0°, (c) Ls = 209.5° and (d) Ls = 210.0° in Mars year 24. The corresponding MGS TES dust optical depth is superimposed. Only the dust opacity retrievals labeled as "good" in TES data (atmospheric_opacity_rating = 0) are used in the plot. (a and b) are consecutive sols, so are (c and d).

optically thick part further north. It is interesting to note that for the opposite fall and winter, in the southern hemisphere, assimilation of TES radiances with the WRF/DART data assimilation system suggests a significant peak in atmospheric dust opacity near the southern cap edge that is also not captured in the TES nadir dust retrievals (Lee et al., 2011). Given that it is possible that the atmosphere may posses dust that the retrievals do not properly capture, we have implemented a simple augmentation to the northern mid/high latitude dust opacity prescription in order to examine how extra dust at these latitudes might influence the simulated $m = 3$ traveling waves.

Our test simulations described below examine if the additional forcing associated with the mid/high latitude curvilinear dust storms can constructively strengthen the $m = 3$ traveling waves for the case of background "MGS dust scenario". This may point to a possible positive feedback since the simulated $m = 3$ traveling waves are associated with relatively stronger near surface wind variations indicative of more effective dust lifting potential, as will be discussed in Section 3. Note that we do not immediately jump to interactive dust simulations because of the extra complexity and uncertainty associated with poorly understood dust lifting, vertical mixing and transport processes. While these will need to be addressed in order to completely simulate the martian atmosphere, the purpose here is merely to test the sensitivity of the northern mid/high latitude $m = 3$ traveling waves to a specific assumed dust distribution.

In Test 1 ("traveling wave dust simulation"), we have added an eastward traveling zonal wavenumber $m = 3$ half-sine wave (i.e., positive additions only, Eq. (1)) with a wave period of $T = 2.2$ sol during Ls = 180–360° to the "MGS dust scenario" (Fig. 3b). The additional dust, $\tau_{\mathrm{add}}(\lambda, \phi, t)$, is prescribed using the following formulation:

$$\begin{aligned} &A(\phi) = 2.0 \cdot \cos((\phi - 60^{\circ})/60^{\circ} \cdot \pi), && 30^{\circ} < \phi < 90^{\circ} \\ &A(\phi) = 0, && \text{otherwise} \\ &\tau_{\mathrm{add}}(\lambda, \phi, t) = \max\left(A(\phi) \cdot \sin\left(\tfrac{\pi m \lambda}{180^{\circ}} - \tfrac{2\pi}{T} t + \varphi_0\right), 0\right) \end{aligned} \tag{1}$$

where λ is longitude in degrees, t is time in sols. $m = 3$ is the zonal wave number. $T = 2.2$ sol is the wave period of the frequently occurring $m = 3$ traveling wave derived from MGS TES data (Banfield

et al., 2004). As will be shown later, it is also among the preferred wave periods of MarsWRF simulated $m = 3$ traveling waves. φ_0 is the phase of the wave-form dust distribution and $\varphi_0 = 0$ is used for the results in Section 4 unless specified otherwise. The amplitude $A(\phi)$ maximizes at 60°N, and decays to zero at 30°N and 90°N according to a cosine function. This crudely represents traveling dust storms associated with $m = 3$ traveling waves at the edge of the polar vortex. It is a simplification that allows us to test the effect of such a forcing at different time during the fall and winter period. It does not mean to imply that these traveling dust storms are constantly present throughout the fall and winter. However, as will be discussed in Section 4, the prescribed traveling dust storms have negligible effect on the simulated $m = 3$ traveling waves during the winter solstice period when curvilinear dust storms are nearly absent in MGS MOC images, but they have substantial effect during the pre- and post-solstice periods when curvilinear dust storms are frequently observed.

The vertical distribution for the additional dust in Test 1 follows that in the "MGS dust scenario" where the additional dust merely represents an increase in the surface total optical depth. As an example, the cumulative dust optical depth profile at 57.5°N and Ls = 217.5° is shown by the dashed line in Fig. 4. The results for Test 1 will be presented in Section 4.1. We have also performed simulations with smaller or fewer traveling dust blobs centered at various latitudes. These results will be mentioned in Section 4.4.

In Test 2 ("zonally uniform dust simulation"), we keep everything else the same as Test 1, but replace the traveling dust blobs with a zonally uniform dust distribution that has the same amount of zonally integrated dust $\tau_{add}(\phi) = A(\phi)/\pi$. This experiment is intended to compare the effect of the additional dust forcing represented by an $m = 3$ traveling half-sine wave versus a zonally uniform amount. Results will be presented in Section 4.2.

In Test 3 ("low dust top wave simulation"), we keep everything else the same as Test 1, but set the "dust top" altitude for the additional dust to 10 km which is lower than that in Test 1. The accumulated dust optical depth profile at 57.5°N and Ls = 217.5° for this case is shown by the dotted line in Fig. 4. Although the total optical depth at the surface is the same as that in Test 1, the rate of decrease with height is much faster. This experiment is motivated by Mars Reconnaissance Orbiter (MRO) Mars Climate Sounder (MCS) observations that suggest near surface confinement of new dust storms at the polar cap edge (McCleese et al., 2010). This behavior was also predicted by Basu et al. (2004, 2006) using the GFDL Mars GCM. Test 3 is intended to test the effect of the vertical dust distribution on the simulated $m = 3$ traveling waves. Results will be presented in Section 4.3.

All the simulations are run for 10 Mars years with output every two hours. The outputs for the last nine years are used for analysis.

3. Standard simulation

The standard MarsWRF simulation compares reasonably with the observed zonal mean state (Richardson et al., 2007). In this section, we investigate the traveling waves simulated by the model. We calculate the standard deviation due to the $1 < T < 10$ sol transient eddies for each latitude and 10-sol time interval. The time mean, trend and diurnal cycle at each grid point within the time interval are removed before analysis. The results for different grid points are averaged zonally and over nine years for presentation. The top row of Fig. 6 shows the standard deviations for the temperature (left) and meridional wind (right) at $\sigma = 0.69$ (approximately 4 km above the surface) as a function of Ls and latitude. The $\sigma = 0.69$ level is used since it is close to the height of the TES observations presented in Section 1. Interpolation onto the 610 Pa level leads to similar results. In agreement with the observations (top row of Fig. 2), there are generally stronger temperature variations before and after the northern winter solstice period.

We extract various wave modes from the transient eddies described above using a Fourier transform. The total Fourier power of the eastward traveling waves whose wave periods are between 1.4 and 10 sols is calculated and used to derive the mean wave amplitudes every 5 sols. The mean wave amplitudes are averaged over nine simulation years for each 5° Ls bin and shown in the bottom three rows of Fig. 6 for zonal wave number $m = 1$, 2 and 3, separately. For both the temperature and meridional wind, all three wavenumbers show stronger variations before and after the northern winter solstice period, and the maximum amplitude of the $m = 2$ waves is larger than that of the $m = 1$ and $m = 3$ waves. However, comparing the left and right columns of Fig. 6, we find that the $m = 1$ waves have substantial amplitudes in the temperature field, but small amplitudes in the meridional wind field, while the $m = 3$ waves have small amplitudes in the temperature field, but appreciable amplitudes in the meridional wind field. A notable difference between the observed (Fig. 2) and simulated (left column of Fig. 6) traveling waves in the temperature field is that the simulated $m = 3$ waves appear much weaker than the $m = 1$ and $m = 2$ waves, while the observed $m = 3$ waves have amplitudes comparable to the $m = 1$ and $m = 2$ waves. Fig. 6 suggests that the $m = 3$ traveling waves may provide even larger near surface wind (and therefore surface stress) variations if the simulated $m = 3$ amplitudes in the near surface temperature increase, which in turn implies that the $m = 3$ waves may play an efficient role in dust lifting at the northern mid/high latitudes during the fall and winter.

The left column of Fig. 7 shows the eddy kinetic energy mass integrated from the surface ($\sigma = 1$) up to $\sigma = 0.1$ (about 25 km altitude) and the corresponding contributions of the eastward traveling $1.4 < T < 10$ sol $m = 1$, 2 and 3 waves. We first calculate the eddy kinetic energy per unit mass $((u'^2 + v'^2)/2)$ at each grid point using the de-trended and diurnal-cycle-removed eddy winds (u' and v') for each 10-sol interval every 5 sols, then do a mass integration from the surface to $\sigma = 0.1$. We calculate the zonal average and time average over the 10-sol interval (top row in the left column of Fig. 7). The integrated eddy kinetic energy is heavily weighted toward the surface due to the density profile. To calculate the contributions of different wave modes (rows 2–4 in the left column of Fig. 7), we use the sum of the total Fourier powers of the $1.4 < T < 10$ sol eastward traveling eddies for the zonal and meridional wind, average them over the corresponding frequency band, and do a mass integration from the surface to $\sigma = 0.1$. All the results are averages over nine simulation years for each 5° Ls bin. The eddy kinetic energy result for $\sigma > 0.1$ (the left column of Fig. 7) echoes the meridional wind result for $\sigma = 0.69$ (the right column of Fig. 6). So, the winter solstice minimum is also present in the vertically integrated eddy kinetic energy for the two first scale heights.

The right column of Fig. 7 shows the results for normalized surface pressure, i.e. the percentage variation of surface pressure. The analysis method is the same as that for temperature in Fig. 6. The pattern of variation is different than that of the other variables. Specifically, north of 65°N, the standard deviations during Ls = 200–220° are smaller than those during Ls = 220–330°, though there is a secondary minimum during Ls = 250–270°. Fig. 7 suggests that it is mainly due to the seasonal behavior of the $m = 1$ traveling waves. The standard simulation suggests that the $m = 1$ traveling waves are important for the surface pressure variations during the winter solstice period, but are not so much for the near surface meridional wind. The winds associated with the simulated $m = 1$ waves are the strongest at upper levels (not shown) and very weak near the surface. The eddy kinetic energy shown in the left column of Fig. 7 is mass integrated from the surface to $z \approx 25$ km and is strongly weighted toward the surface. As a result, the

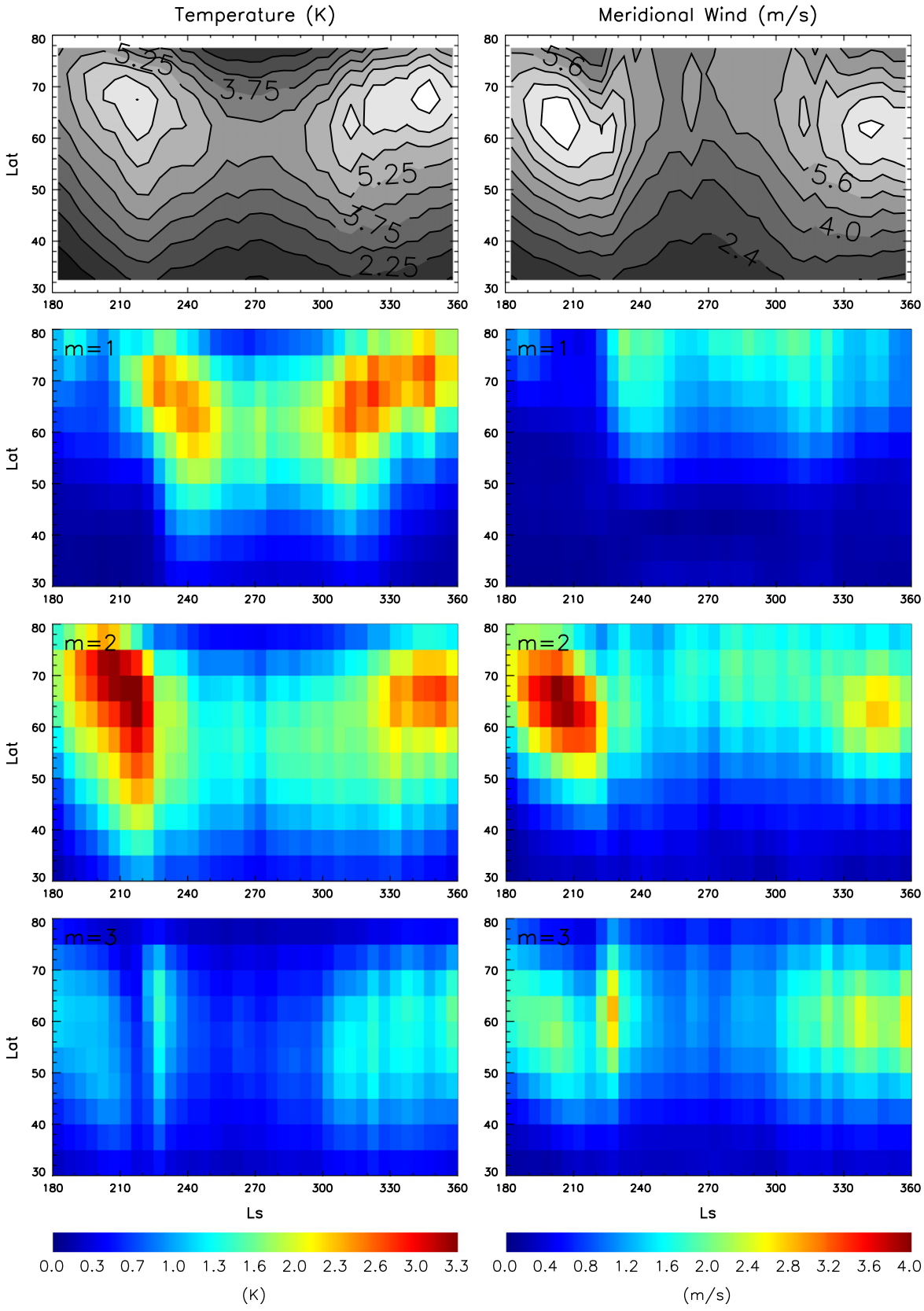

Fig. 6. The seasonal evolution of the transient eddies at $\sigma = 0.69$ (about 4 km high, model level 5) for the standard simulation in terms of the (left) temperature and (right) meridional wind field. (Row 1) The standard deviations of the $1 < T < 10$ sol transient eddies as a function of Ls and latitude. (Rows 2–4) The Ls versus latitude distribution of the spectrally averaged amplitude of the $1.4 < T < 10$ sol eastward traveling zonal wave number $m = 1$, 2 and 3 waves.

pattern shown by the left and right column of Fig. 7 is different. For the simulated $m = 3$ traveling waves, the seasonal pattern in the surface pressure field is similar to that in the temperature, near surface meridional wind and eddy kinetic energy. The standard

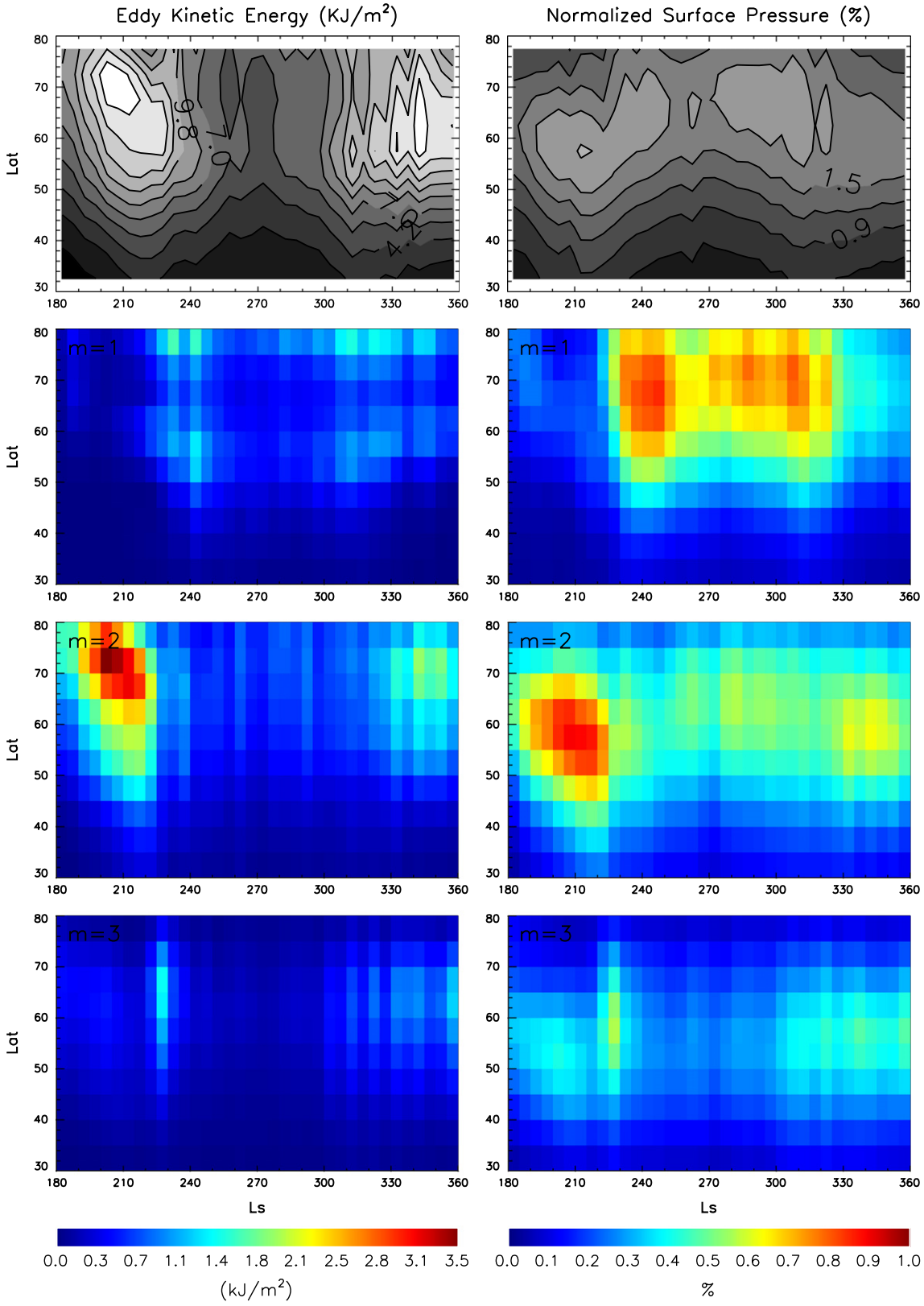

Fig. 7. The seasonal evolution of the transient eddies for the standard simulation in terms of the (left) mass integrated eddy kinetic energy from the surface to $\sigma = 0.1$ (about 25 km altitude) and (right) normalized surface pressure. (Row 1) The standard deviations of the $1 < T < 10$ sol transient eddies as a function of Ls and latitude. (Rows 2–4) The Ls versus latitude distribution of the spectrally averaged amplitude of the eastward traveling $1.4 < T < 10$ sol zonal wave number $m = 1$, 2 and 3 waves.

simulation shows that different wave numbers have different properties and calls for caution about which variable and location are used when the relative strength of the waves is evaluated.

The results in Figs. 6 and 7 are averaged over the wave frequency band. The spectral composition of the eastward traveling $1 < T < 10$ sol waves in the temperature field at $\sigma = 0.69$ and

52.5°N is shown in the top row of Fig. 8. The amplitudes of the $m = 1$, 2 and 3 waves are plotted as a function of wave period (sol) and Ls. Fig. 8 only shows the eastward traveling waves since the westward traveling waves in this frequency range and location are negligible in the simulation. The dominant wave periods in the simulation are $T = 4$–10 sol for $m = 1$ waves ($T > 10$ sol waves are filtered out), $T = 2.5$–4 sol for $m = 2$ waves, and $T = 1.5$–4 sol for $m = 3$ waves. The waves with shorter wavelengths generally have shorter wave periods. These results are largely consistent with the MGS TES observations (Banfield et al., 2004) and previous GCM simulations (Barnes et al., 1993; Basu et al., 2006; Wilson et al., 2006). The wave period used for the idealized dust forcing ($T = 2.2$ sol) in Test 1 and Test 3 is among the preferred wave periods of the simulated $m = 3$ traveling waves.

The standard simulation successfully reproduces the observed traveling wave modes and the stronger temperature variations before and after the northern winter solstice period. However, the simulated $m = 3$ traveling waves in the standard simulation appear to be much weaker than what the TES data suggest they are. Due to the importance of the $m = 3$ traveling waves to the dust cycle inferred from the observations (Section 1), and the potential of the $m = 3$ waves in lifting dust as implied by the standard simulation (Fig. 6), we will study the structure and dynamics of the simulated

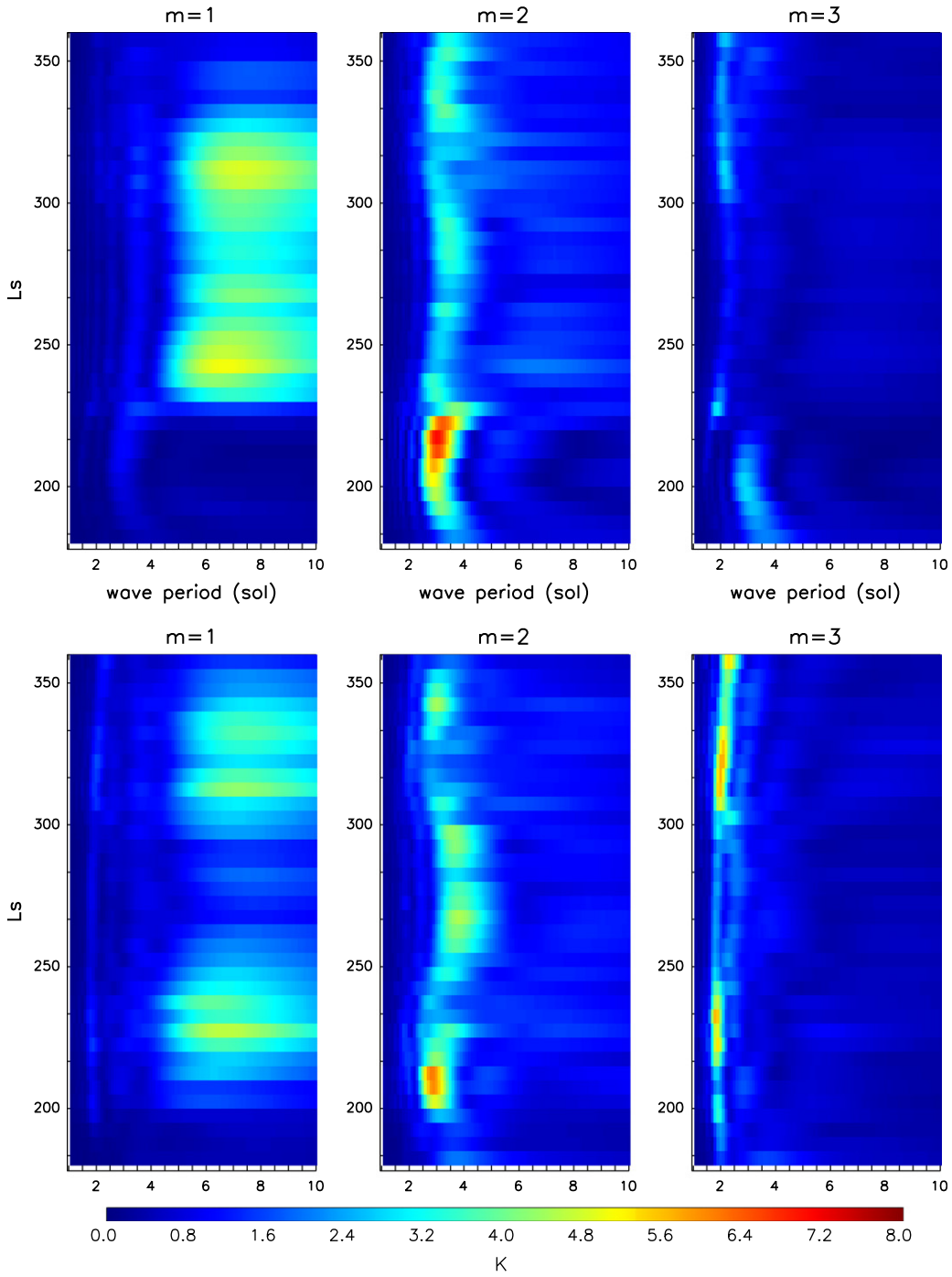

Fig. 8. The amplitude of the eastward traveling zonal wave number (left) $m = 1$, (middle) $m = 2$ and (right) $m = 3$ waves in the temperature field at $\sigma = 0.69$ and 52.5°N as a function of wave period and Ls for (top) the standard simulation and (bottom) Test 3 – the low dust top wave forcing simulation.

$m = 3$ traveling waves and investigate a possible mechanism for enhancing these waves in the next section.

4. Simulations with additional dust forcing

4.1. Test 1 – Traveling wave dust simulation

Observations show that the $m = 3$ traveling waves are prominent during the periods of active flushing dust storms, indicating that the traveling dust storms neglected in the "MGS dust scenario" may play a role in exciting/maintaining these waves. To test this hypothesis, we have performed the traveling wave dust simulation (Test 1) and analyzed the result in the same way as we analyzed the standard simulation.

Results for the temperature and meridional wind at $\sigma = 0.69$ are shown in Fig. 9 in the same format as that for Fig. 6. The familiar pattern of the winter solstice minimum is still present here. However, in the temperature field, the $m = 3$ traveling waves during Ls = 220–240° and Ls = 305–340° are generally about 20–80% stronger than those in the standard simulation. A paired Student's t-test for the Null hypothesis (H_0) that the $m = 3$ traveling waves for Test 1 and the standard simulation are of the same strength shows that the Null hypothesis should be rejected at $\alpha = 0.05$ significance level for these time periods, i.e., that the increase in Test 1 relative to the standard simulation is statistically significant. It is interesting that the most significant enhancement in Test 1 occurs at approximately the same time periods when the MOC images show active flushing dust storms. Little enhancement is found for the winter solstice period. The simulated $m = 3$ traveling waves are accompanied by the $m = 1$ (with some $m = 2$) waves within the same latitude band and time periods. The simulated $m = 1$ traveling waves also have substantial amplitudes north of 65°N where the simulated $m = 3$ traveling waves are almost absent. The simulated $m = 2$ traveling waves peak before Ls = 220° and after Ls = 330°.

In the meridional wind field, Fig. 9 shows that the simulated $m = 3$ traveling waves are the major contributors to the variability south of about 70°N during Ls = 220–240° and Ls = 305–340°. The $m = 2$ traveling waves dominate the variability before Ls = 220° and after Ls = 330°. The $m = 1$ traveling waves mainly contribute to the variability north of about 70°N, but their maximum amplitude is smaller than that of the $m = 2$ and $m = 3$ traveling waves south of 70°N. Lewis et al. (2008) presented the standard deviation of the meridional wind at 400 Pa using a Mars data assimilation product. Compared with their result, the meridional wind variation in Test 1 shows the same seasonal pattern but is approximately 20–40% weaker. Both the near surface eddy kinetic energy and eddy momentum flux simulated in Test 1 also have a pre- and a post-solstice maximum, and the simulated $m = 3$ traveling waves make major contributions to them during Ls = 220–240° and Ls = 305–340° (not shown).

Fig. 10 shows the latitude versus vertical model level number/height cross sections of the transient temperature variations in Test 1 at Ls = 222.5°, 267.5° and 322.5°, representing the pre-solstice, solstice and post-solstice period, respectively. The simulated $1 < T < 10$ sol transient temperature standard deviations are shown in the left column. They include contributions from all the transient eddies within the frequency band. The simulated spectrally averaged amplitudes of the eastward propagating $1.4 < T < 10$ sol $m = 3$ waves in the temperature field are shown in the right column. They are calculated in the same way as that for Fig. 9, but are presented here to show the vertical structure. The vertical axis is linear in model level number (on the left hand side) to emphasize the region near the surface where the $m = 3$ traveling waves are the strongest. The corresponding height (km) for each model level is labeled on the right hand side. The simulated zonal mean temperature contours are superimposed.

Fig. 10 shows that the simulated zone of strong transient temperature variation follows the edge of the polar vortex indicated by the sharp latitudinal temperature gradient. Although not the topic of this study, the simulated temperature variations above about 20 km are strong throughout the fall and winter, and are at their maximum during the winter solstice period. This is very different than the seasonal behavior of the simulated transient eddies at lower levels. The simulated eastward traveling $1.4 < T < 10$ sol $m = 3$ waves in the temperature field are confined below about 15 km, and make significant contributions to the transient temperature variations near the surface. They exhibit a strong–weak–strong pattern as the season progresses from Ls = 180° through Ls = 270° to Ls = 360°. Fig. 10 indicates that the winter solstice minimum of the $m = 3$ waves in the temperature field is valid for all the model levels within the first scale height or so and is most apparent at a height of about 2 km which is closer to the surface than the $\sigma = 0.69$ level used for Fig. 9. Compared with the results for traveling waves derived from TES data (Banfield et al., 2004), the simulation qualitatively captures the observed strong–weak–strong seasonality of the near surface temperature variation and the vertical confinement of the $m = 3$ traveling waves in the temperature field. The observed upper level transient eddies appear to be related to major dust storms (Banfield et al., 2004; Wilson et al., 2002) which we do not consider. So the difference between the model and observation in the timing of the upper level maximum is not surprising. Nevertheless, the model suggests a marked difference between the lower and upper level transient eddies, which agrees qualitatively with the observation (Banfield et al., 2004).

Fig. 11 shows the latitude versus height plot of the Eliassen–Palm (EP) fluxes (arrows) and their divergences (colors) for the transient eddies in Test 1 at Ls = 227.5°, 267.5° and 322.5°, respectively. The left column is for all the $1 < T < 10$ sol transient eddies, including both eastward and westward propagating waves of various zonal wavenumbers. The right column is for the eastward propagating $1.4 < T < 10$ sol $m = 3$ waves only. The EP flux formula for the primitive equation in spherical log-pressure coordinate (Andrews et al., 1987) is used in the calculation. The EP fluxes and their divergences are much stronger at Ls = 227.5° and 322.5° than at Ls = 267.5°. The EP fluxes associated with the $1 < T < 10$ sol transient eddies (with various zonal wave numbers) direct upward and equatorward throughout the column within 50–70°N, and poleward above about 40 km within 20–50°N. There is substantial zonal wind acceleration (up to about ±10 m/s/sol) associated with these waves. The EP fluxes associated with the eastward propagating $1.4 < T < 10$ sol $m = 3$ waves are confined within the first two scale heights or so, which is consistent with the distribution of the corresponding temperature perturbation (Fig. 10). They direct upward and equatorward within 50–70°N, and make significant contributions to the overall wave activity near the surface. Fig. 11 also indicates that the upper level wave activity shown in the left column is mostly due to waves other than the eastward traveling $1.4 < T < 10$ sol $m = 3$ waves. The EP flux plots for the simulated $m = 1$ and $m = 2$ traveling waves (not shown) have large values at the upper levels, which is consistent with the finding by Banfield et al. (2004) that the observed $m = 1$ and $m = 2$ traveling waves derived from TES temperature data have large amplitudes at upper levels.

In Fig. 12, we examine the energetics of the eastward propagating $1.4 < T < 10$ sol $m = 3$ waves simulated in Test 1 at Ls = 227.5°, 267.5° and 322.5°. The formulation in the appendix of Ulbrich and Speth (1991) is used in this study. Fig. 1 of Ulbrich and Speth (1991) shows a diagram for this six-box energy cycle. The eddy available potential energies can be generated from the flow or external forcing. The eddy perturbations are derived in the same

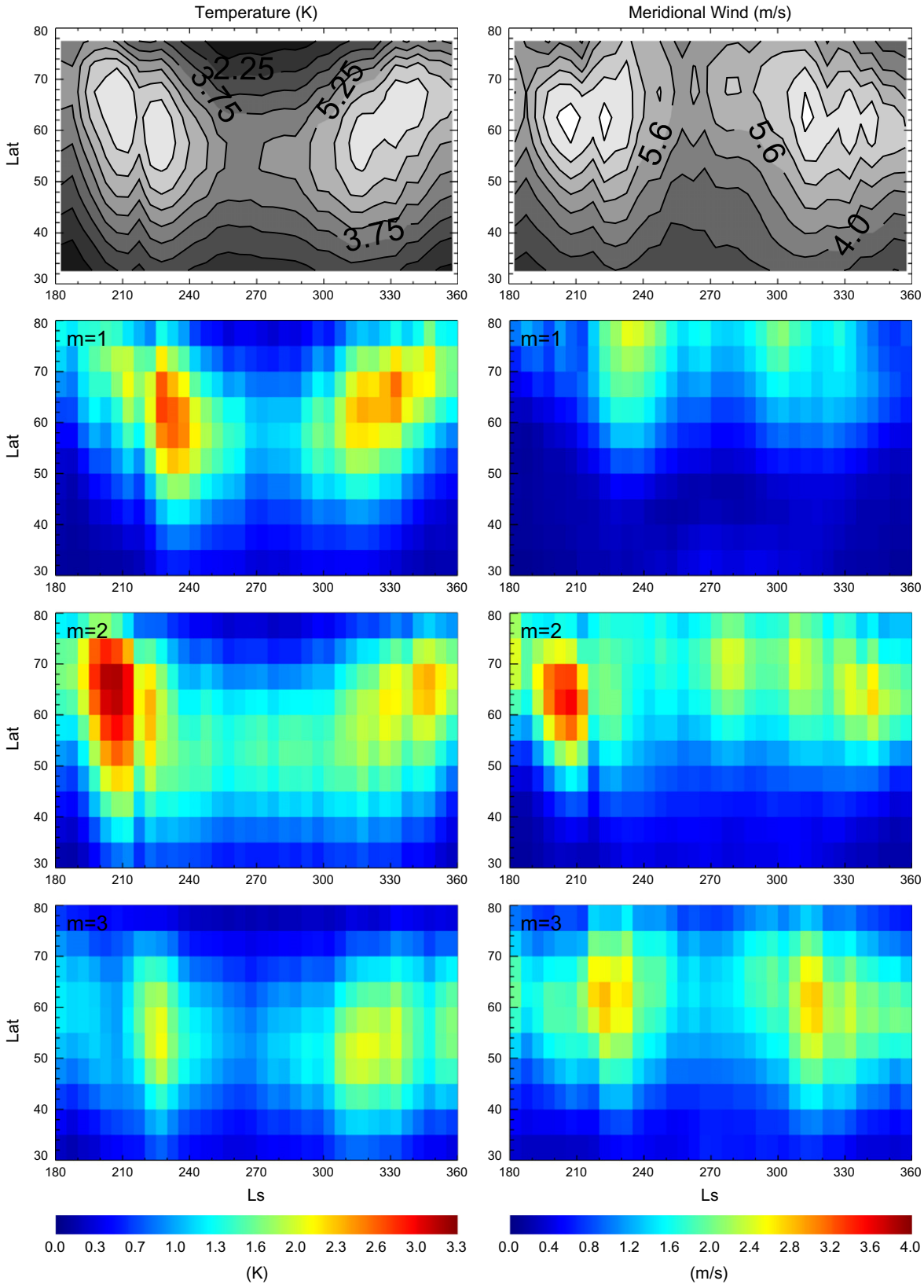

Fig. 9. The seasonal evolution of the transient eddies at $\sigma = 0.69$ (about 4 km high) for Test 1 – the traveling wave dust simulation in terms of the (left) temperature and (right) meridional wind. (Row 1) The standard deviations of the $1 < T < 10$ sol transient eddies as a function of Ls and latitude. (Rows 2–4) The Ls versus latitude distributions of the spectrally averaged amplitudes of the $1.4 < T < 10$ sol eastward traveling zonal wave number $m = 1$, 2 and 3 waves.

way as those in the bottom row of Fig. 9. The left column of Fig. 12 shows the eddy available potential energy (contour) and the conversion rate from the eddy available potential energy to the eddy kinetic energy (color). The right column shows the eddy kinetic

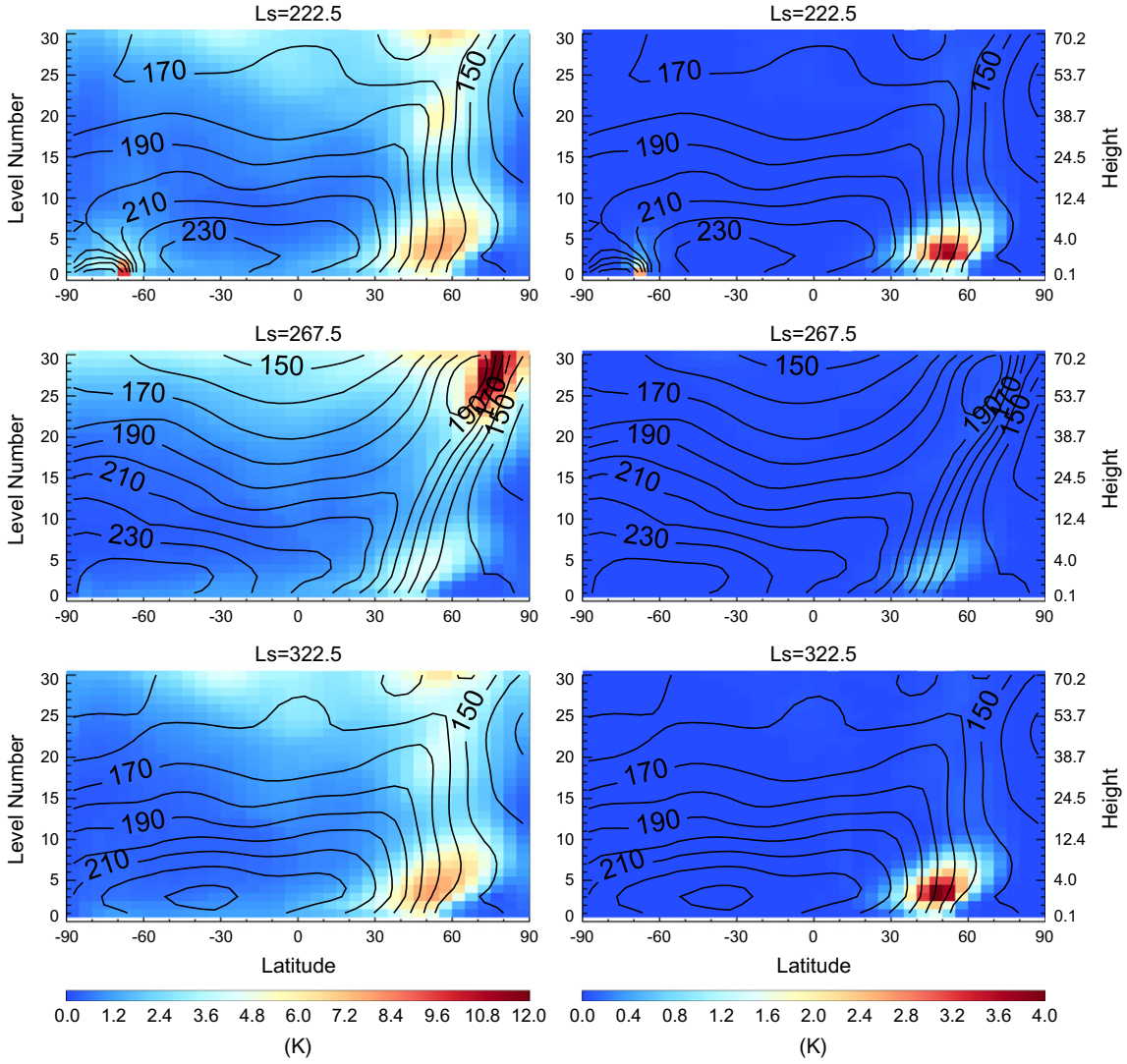

Fig. 10. The latitude versus vertical model level number (left axis)/height (right axis) cross sections of (left column) the $1 < T < 10$ sol transient eddy temperature standard deviations and (right column) the mean amplitudes of the eastward traveling $1.4 < T < 10$ sol zonal wave number $m = 3$ waves in the temperature field at (top row) Ls = 222.5°, (middle row) Ls = 267.5° and (bottom row) Ls = 322.5° for Test 1 – the traveling wave dust simulation. Only the lowest 30 model levels are plotted. The approximate height (km) for each model level is labeled on the right hand side. The simulated zonal mean temperature contours are superimposed.

energy (contour) and the conversion rate from the zonal kinetic energy to the eddy kinetic energy (color).

Fig. 12 shows that the eastward propagating $1.4 < T < 10$ sol $m = 3$ waves generate their kinetic energy baroclinicly near the surface through warm air rising and cold air sinking, and decay through horizontal transfer of eddy kinetic energy to the zonal mean flow. The energy conversion rates are large for the pre- and post-winter solstice periods, so are the eddy available potential energy and eddy kinetic energy. The eddy available potential energy exhibits a near surface maximum, which is consistent with the distribution of the corresponding temperature perturbation in the right column of Fig. 10. Before and after the northern winter solstice, the eddy kinetic energy occupies a deep vertical column within 40–80°N, with a local maximum at a height between 5 km and 15 km.

To get an idea of why the eddy kinetic energy extends higher than the eddy available potential energy in Fig. 12, we plot in Fig. 13 the latitude versus height distributions of the amplitudes of the eastward propagating $1.4 < T < 10$ sol $m = 3$ winds at Ls = 227.5°, 267.5° and 322.5°. The left column is for the zonal wind component (u') and the right column is for the meridional wind component (v'). The corresponding zonal mean zonal and meridional winds for Test 1 are superimposed. The wave amplitudes are derived in the same way as those for temperature in the right column of Fig. 10.

Fig. 13 shows that the simulated eastward propagating $1.4 < T < 10$ sol $m = 3$ eddy winds are strong before and after the northern winter solstice. The seasonality is in agreement with the pattern shown in Fig. 12. Different than the eddy temperatures which are confined within the first two scale heights or so (Fig. 10), the eddy winds are distributed within a deep column at the poleward side of the circumpolar jet and the overturning Hadley cell. The v' component is generally stronger than the u' component, and maximizes at a height between 10 km and 30 km. As a result, the eddy kinetic energy of the eastward propagating $1.4 < T < 10$ sol $m = 3$ waves has a deeper structure than the corresponding temperature perturbation and eddy available potential energy.

Using the MGS Radio Science (RS) data, Hinson (2006) derived the vertical structure of temperature and geopotential height for the eastward propagating $T = 2.3$ sol $m = 3$ wave. He showed that the eddy temperature amplitude was mostly concentrated in the lowest scale height and that the eddy geopotential height

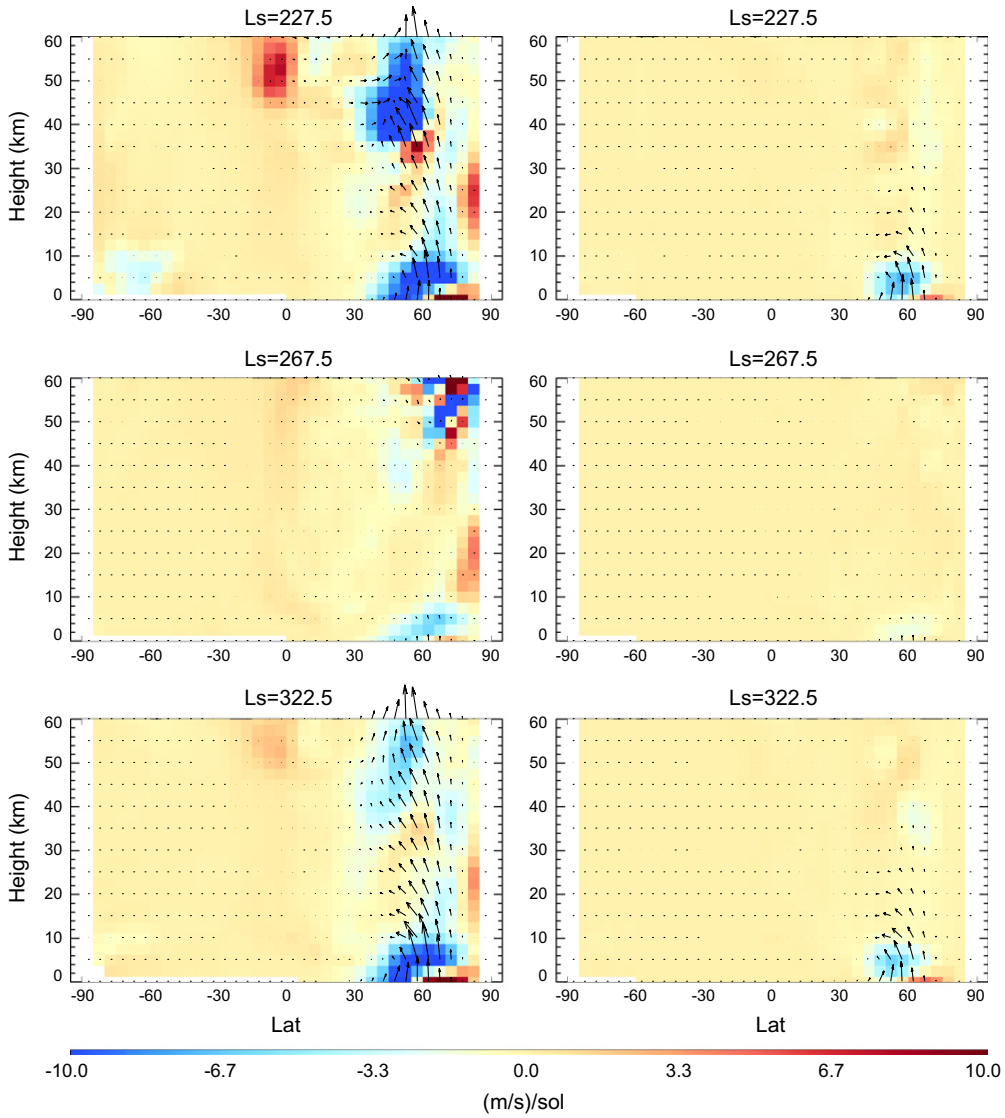

Fig. 11. The latitude versus height plot of the EP flux (arrow) and its divergence (color) at (top row) Ls = 227.5°, (middle row) Ls = 267.5° and (bottom row) Ls = 322.5° for Test 1 – the traveling wave dust simulation. The left column is for all the $1 < T < 10$ sol transient eddies. The right column is for the eastward traveling $1.4 < T < 10$ sol $m = 3$ waves. The lowest 60 km is plotted in each panel. The vertical component of the EP flux is scaled by 50 for plotting. (For interpretation of the references to color in this figure legend, the reader is referred to the web version of this article.)

amplitude increased with the altitude. Furthermore, he showed that the eddy geopotential height tilted westward with height near the surface but had little phase tilt above. His result is indicative of a wave mode that is highly baroclinic near the surface and more barotropic above. Such a structure was previously modeled by Barnes et al. (1993). Our simulated near surface confinement of eddy temperature and vertically extended eddy winds are consistent with such an eddy structure.

We investigate the difference in the zonal mean temperature structure between the standard simulation (black line) and Test 1 (red line) in the left column of Fig. 14. Representative latitude versus height cross sections for the pre-solstice (Ls = 222.5°), solstice (Ls = 267.5°) and post-solstice (Ls = 322.5°) periods are shown. The temperature structure below about 40 km (level 20) remains almost the same south of about 30°N between the two simulations. The temporal evolution of the thermal structure (for either the standard simulation or Test 1) indicates that the $m = 3$ traveling waves are stronger when the isotherms at the polar vortex edge are oriented more vertically (corresponding to a smaller lapse rate). Due to the inclusion of the traveling dust blobs in Test 1, for the pre- and post-solstice period, the latitudes between 40°N and 80°N are colder below about 12 km (level 10) in Test 1 than in the standard simulation, especially in the 5–10 km height range, and are warmer above about 25 km (level 15). Consequently, the near surface inversions at the polar vortex edge for these time periods are less pronounced in Test 1 than in the standard simulation.

The difference in the thermal structure between Test 1 and the standard simulation leads to a difference in the baroclinic parameter $((\partial u/\partial z)/N)$, which is defined as the wind shear in the vertical $(\partial u/\partial z)$ divided by the static stability (N). Read et al. (2011) found this parameter to be useful for indicating the strength of baroclinic eddies in the northern hemisphere. Fig. 15 shows the seasonal variation of the baroclinic parameter in our simulations. The triangles are the averages over the region between 30°N and 75°N and from the surface to about 10 km (level 9). The dots are the 90% percentiles for the same region and show a similar seasonal pattern as that shown by the triangles. The zone of the sharpest near surface latitudinal temperature gradient (Fig. 14) is included in this region.

Fig. 15 shows that both the standard simulation (black) and Test 1 (red) have local maximum in the baroclinic parameter before and

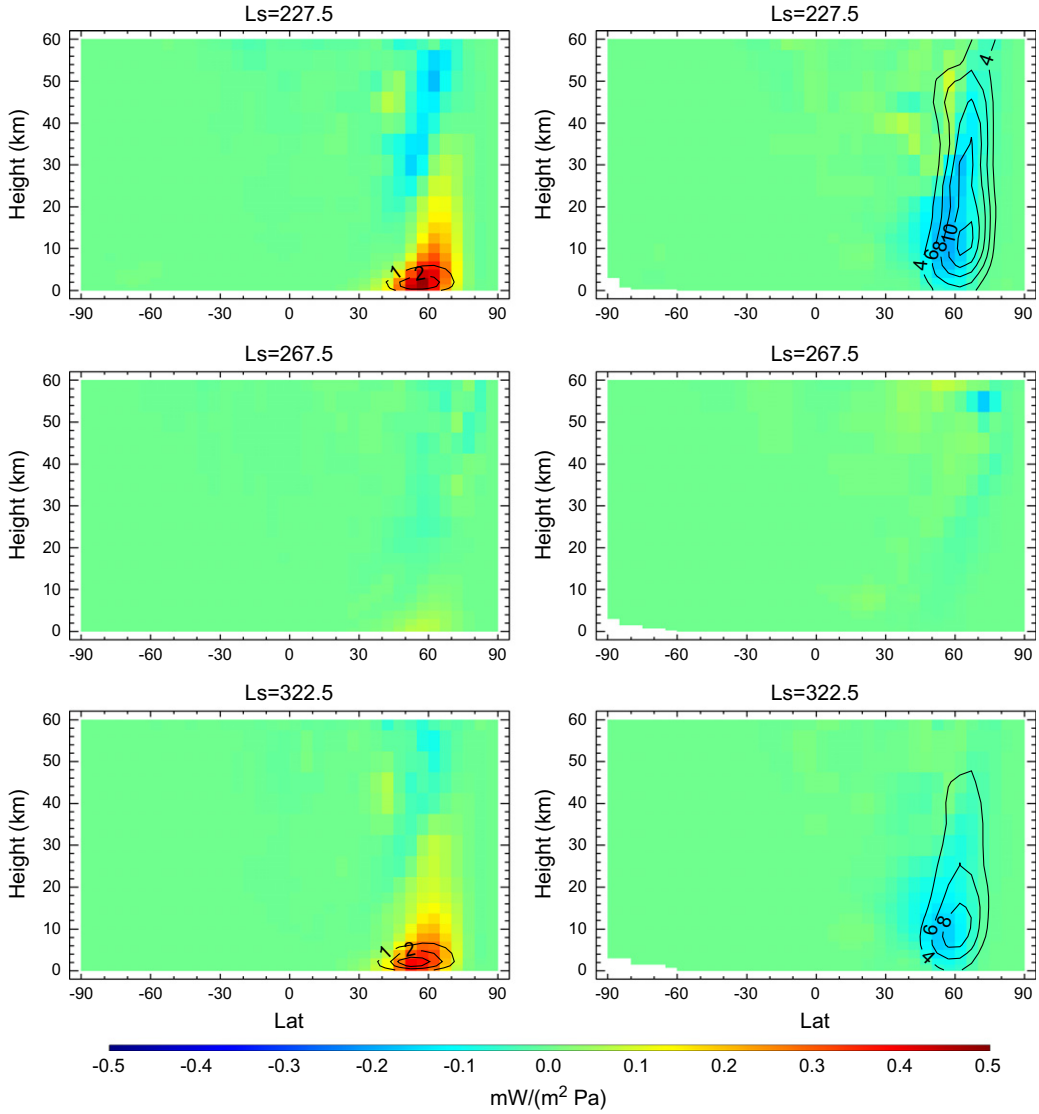

Fig. 12. The latitude versus height distribution of selected components of the energy cycle defined in Ulbrich and Speth (1991) at (top row) Ls = 227.5°, (middle row) Ls = 267.5° and (bottom row) Ls = 322.5° for the simulated eastward traveling $1.4 < T < 10$ sol $m = 3$ waves in Test 1 – the traveling wave dust simulation. For panels in the left column, the color shows the energy conversion rate (mW/m^2 Pa) from the eddy available potential energy to the eddy kinetic energy, the contour shows the eddy available potential energy (J/m^2 Pa). For the panels in the right column, the color shows the energy conversion rate from the zonal kinetic energy to the eddy kinetic energy (mW/m^2 Pa), the contour shows the eddy kinetic energy (J/m^2 Pa). The lowest 60 km is plotted in each panel.

after the northern winter solstice. The seasonal pattern exhibited by the baroclinic parameter is consistent with that shown by the simulated temperature and meridional wind (Figs. 6 and 9). Test 1 has larger baroclinic parameter and stronger $m = 3$ traveling waves than the standard simulation for the pre- and post-solstice periods. This suggests that larger baroclinic parameter may be favorable for $m = 3$ traveling waves in the simulation. However, the difference in the baroclinic parameter is only a few percent. As will be discussed later, changes in this parameter is not the only factor affecting the strength of the simulated $m = 3$ traveling waves.

In Fig. 16, we examine how changes in the zonal mean structure affect the related energy conversion rates. Again, the formulation of Ulbrich and Speth (1991) is used. Fig. 16 shows the energy conversion rates at $\sigma = 0.69$ as a function of Ls and latitude for various simulations. The contours show the conversion rates from the zonal available potential energy to the eddy available potential energy for the eastward traveling $1.4 < T < 10$ sol $m = 3$ waves, and the colors show the corresponding conversion rates from the eddy available potential energy to the eddy kinetic energy. The conversion rates are much stronger in Test 1 (Fig. 16b) than in the standard simulation (Fig. 16a), which is consistent with the larger amplitudes of the $m = 3$ traveling waves in Test 1.

4.2. Test 2 – Zonally uniform dust simulation

To investigate the effect of the zonally uniform versus the wave-form dust forcing, we compare the results from the zonally uniform dust simulation (Test 2) with those from the traveling wave dust simulation (Test 1). The Ls versus latitude distribution of the mean amplitude of the eastward traveling $1.4 < T < 10$ sol $m = 3$ waves in temperature is shown in Fig. 17c. For easy comparison, the corresponding plots for other simulations are also shown. Compared with Test 1 (Fig. 17b), the temperature perturbation in Test 2 is slightly weaker for the pre-solstice period, but significantly weaker for the post-solstice period (though still stronger than that in the standard simulation). This suggests that the enhancement of the $m = 3$ traveling waves in the pre-solstice

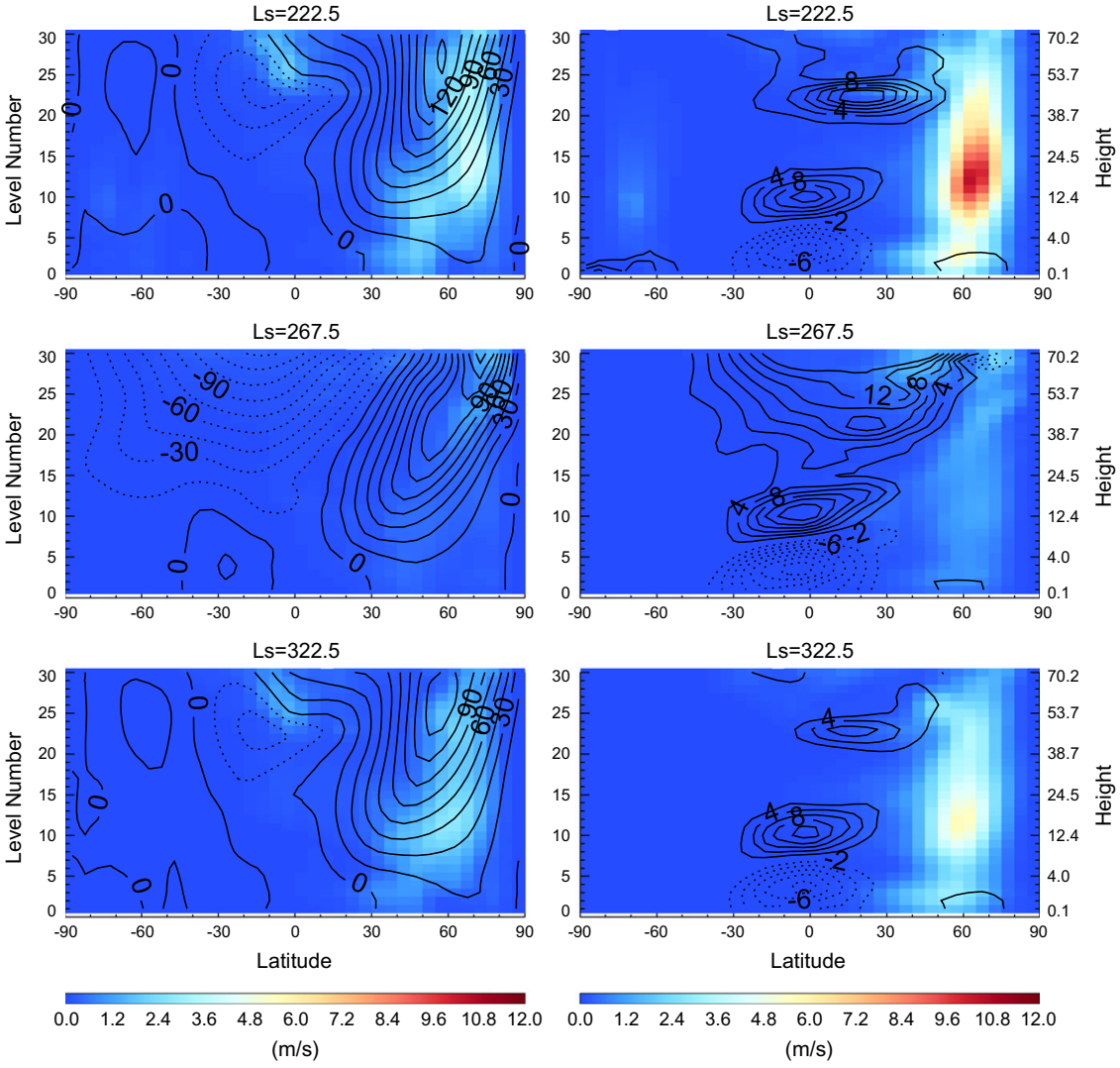

Fig. 13. The latitude versus height cross sections of the amplitudes of the eastward traveling $1.4 < T < 10$ sol $m = 3$ waves in the (left column) zonal wind and (right column) meridional wind field at (top row) Ls = 222.5°, (middle row) 267.5° and (bottom row) 322.5° for Test 1. The corresponding simulated zonal mean zonal and meridional wind contours are superimposed.

period is largely due to the presence of dust within the 30–90°N band (maximizing at 60°N), but the enhancement of the $m = 3$ traveling waves in the post-solstice period in Test 1 is closely related to the specific wave-form dust forcing.

The zonal mean temperature structures for Test 2 are shown by the blue contours in the right column of Fig. 14. They are almost identical to those for Test 1 (the red contours) except for the lowest 1–2 scale heights at the northern mid/high latitudes during the pre- and post-solstice periods. Compared to Test 1, the near surface temperature inversion in Test 2 is even more muted during these periods which would seem to imply stronger $m = 3$ waves. However, the simulated $m = 3$ waves in Test 2 are actually weaker than those in Test 1, especially for the post-solstice period. This suggests that, besides the zonal mean structure, the form of the dust forcing is also a factor influencing the strength of the simulated $m = 3$ traveling waves.

Another hint of the effect of the wave-form dust forcing can be inferred from Fig. 15. For the pre-solstice period, the baroclinic parameter for Test 2 (blue) is larger than that for Test 1 (red), which would seem to imply that the simulated $m = 3$ traveling waves in Test 2 to be stronger. On the contrary, results show that the simulated $m = 3$ traveling waves in Test 2 are slightly weaker than those in Test 1. Therefore, the baroclinic parameter is not the only factor affecting the simulated $m = 3$ traveling waves. For the post-solstice period, the simulated $m = 3$ traveling waves in Test 2 are weaker than those in Test 1 which is consistent with the 90% percentile of baroclinic parameter for Test 2 being smaller. However, the domain averaged baroclinic parameter for Test 2 is almost the same as that for Test 1, indicating that the consistency between the simulated $m = 3$ traveling waves and the baroclinic parameter also depends on how the baroclinic parameter is calculated.

4.3. Test 3 – Low dust top wave forcing

To investigate the effect of dust vertical distribution on the simulated $m = 3$ traveling waves, we analyze the outputs from the low dust top wave forcing simulation (Test 3) where the prescribed additional dust has a "dust top" altitude of 10 km and everything else remains the same as that for the traveling wave dust simulation (Test 1). The mean amplitude of the eastward traveling $1.4 < T < 10$ sol $m = 3$ waves in the temperature field at $\sigma = 0.69$ for Test 3 is shown in Fig. 17d. In comparison with Test 1 (Fig. 17b), the $m = 3$ traveling waves in temperature are further

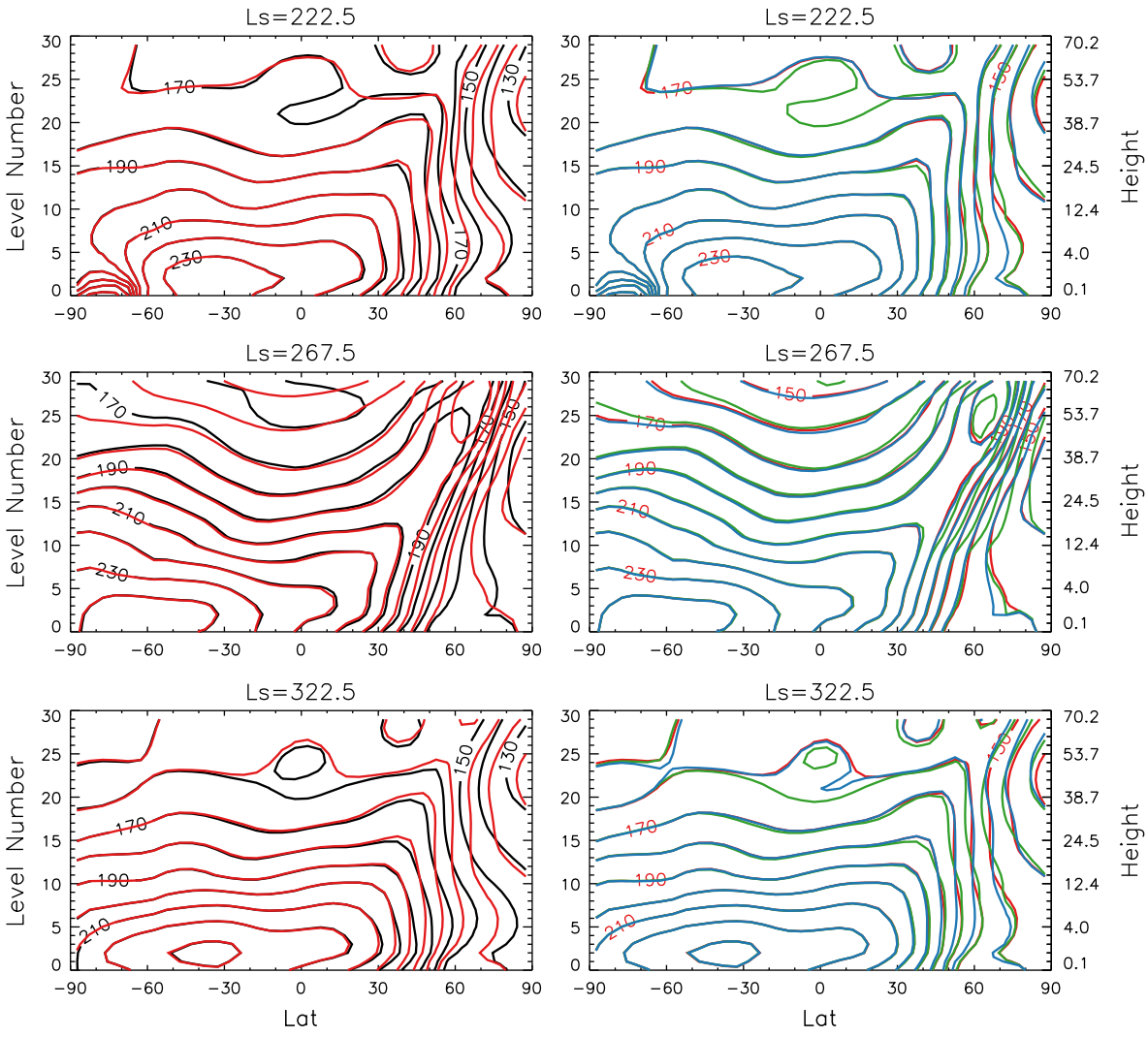

Fig. 14. The latitude versus model level number/height cross section of the zonal mean temperature (K) at (top row) Ls = 222.5°, (middle row) Ls = 267.5° and (bottom row) Ls = 322.5° for various simulations. The lowest 30 model levels are plotted. The model level number is labeled on the left hand side. The corresponding height (km) is labeled on the right hand side. For the panels in the left column, the black contour is for the standard simulation and the red contour is for Test 1. For the panels in the right column, the red contour is for Test 1, the blue contour is for Test 2 and the green contour is for Test 3. (For interpretation of the references to color in this figure legend, the reader is referred to the web version of this article.)

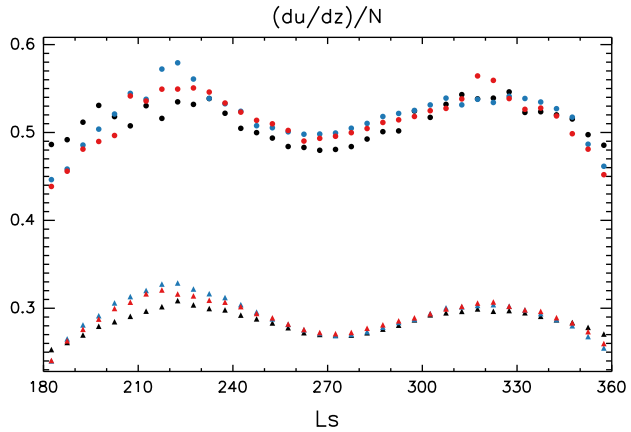

Fig. 15. The seasonal evolution of the baroclinic parameter for the region between 30°N and 75°N from the surface to $\sigma = 0.38$ (~10 km) for (black) the standard simulation, (red) Test 1 and (blue) Test 2. The triangles are the averages and the dots are the 90% percentiles for the domain. (For interpretation of the references to color in this figure legend, the reader is referred to the web version of this article.)

enhanced for both the pre-solstice and post-solstice periods, suggesting that the $m = 3$ traveling waves are stronger when dust is confined closer to the surface. The simulated $m = 3$ traveling waves at $\sigma = 0.69$ in Test 3 are now comparable to or only slightly weaker than the $m = 1$ and $m = 2$ traveling waves in the near surface temperature field, and comparable to or slightly stronger than the $m = 1$ and $m = 2$ traveling waves in the near surface meridional wind field (not shown).

The wave spectra of the eddy temperature at $\sigma = 0.69$ and 52.5°N for Test 3 are shown in the lower panels of Fig. 8. The dominant modes for $m = 1$ and $m = 2$ traveling waves are largely the same as those in the standard simulation, but the $1.5 < T < 2.5$ sol $m = 3$ traveling waves are apparently enhanced in Test 3.

The zonal mean temperature structures for Test 3 are shown by the green contours in the right column of Fig. 14. The largest differences with Test 1 (red) lie above about 15 km for Ls = 267.5° when the simulated $m = 3$ traveling waves are minimal. Below about 15 km, the temperature structures are almost identical to those in Test 1 (red). Consequently, the baroclinic parameters for Test 3 will coincide with those for Test 1 (red dots) in Fig. 15 had they been plotted. Despite the similarities in the zonal mean structure

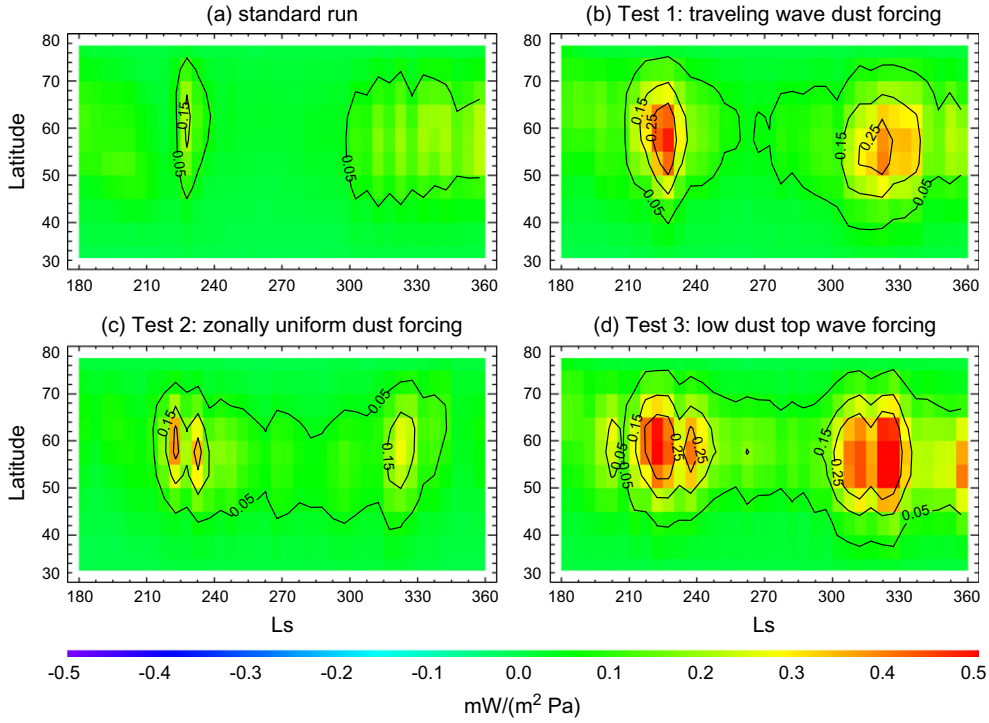

Fig. 16. The Ls versus latitude distribution of selected component of the energy cycle defined in Ulbrich and Speth (1991) at $\sigma = 0.69$ for the eastward traveling $1.4 < T < 10$ sol $m = 3$ waves in (a) the standard simulation, (b) Test 1, (c) Test 2 and (d) Test 3. The color shows the energy conversion rate (mW/m^2 Pa) from the eddy available potential energy to the eddy kinetic energy. The contour shows the energy conversion rate (mW/m^2 Pa) from the zonal available potential energy to the eddy available potential energy.

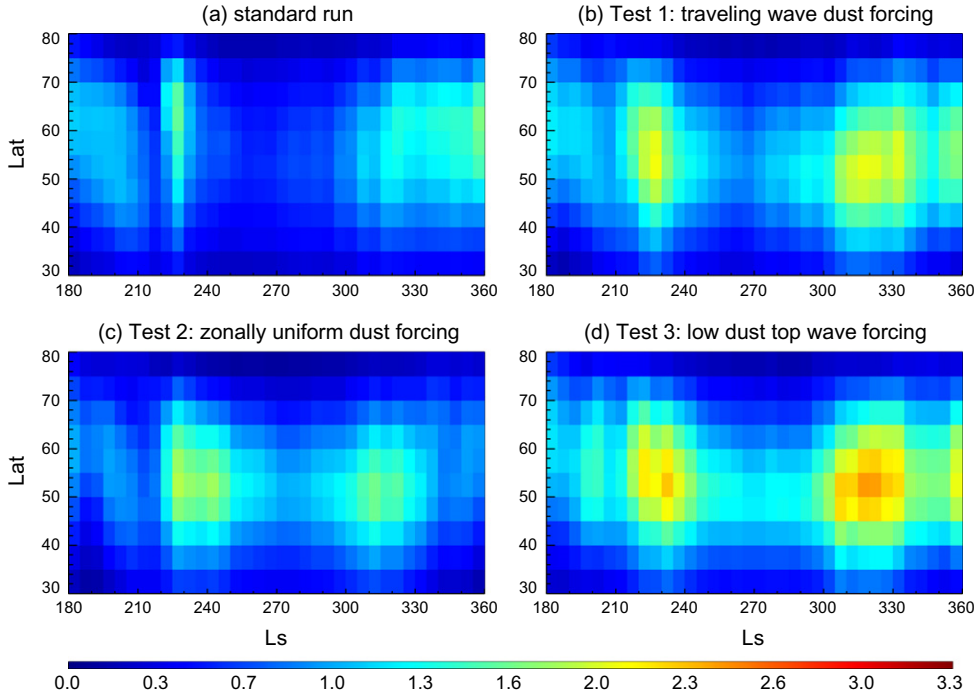

Fig. 17. The Ls versus latitude distributions of the mean amplitudes (K) of the eastward traveling $1.4 < T < 10$ sol $m = 3$ waves in the temperature field at $\sigma = 0.69$ simulated in (a) the standard simulation, (b) Test 1, (c) Test 2 and (d) Test 3.

near the surface, Test 3 has substantially stronger $m = 3$ traveling waves than Test 1, again indicating that changes in the zonal mean structure and the corresponding baroclinic parameter can only partly explain the enhancement of the simulated $m = 3$ traveling waves. In terms of the energy cycle, the conversion rate from the zonal available potential energy to the eddy available potential energy and that from the eddy available potential energy to the eddy kinetic energy are both greater in Test 3 (Fig. 16d) than in Test 1

(Fig. 16b). This also suggests that factors other than the zonal mean state are influencing the simulated $m = 3$ traveling waves.

In addition to the energy conversion from the zonal available potential energy, the eddy available potential energy can also be generated through external forcing (Ulbrich and Speth, 1991). Fig. 18 shows the mean amplitude of the eastward traveling $1.4 < T < 10$ sol $m = 3$ wave forcing at $\sigma = 0.69$ expressed in atmospheric net heating rate as a function of Ls and latitude for Test 1 and Test 3. The net heating rate is the sum of the visible and infrared heating rate due to dust and CO_2. Fig. 18 shows that the strongest $m = 3$ forcing in the model occurs before Ls $\approx 220°$ north of about 55°N where the simulated $m = 2$ waves are dominant (Figs. 6 and 9). The $m = 3$ forcing is also strong within 40–55°N during Ls = 240–300° when the simulated traveling waves near the surface are suppressed (Figs. 6 and 9). Both cases are outside the region and period of interest for the simulated $m = 3$ traveling waves. The imposed $m = 3$ forcing due to the prescribed traveling dust blobs does not affect the simulated $m = 3$ traveling waves much for these irrelevant time periods. However, for the 40–60°N region where the $m = 3$ traveling waves are frequently observed in TES data, we find that the $m = 3$ forcing is quite small during the pre-solstice period (Ls = 210–230°), but appreciable during the post-solstice period (Ls = 300–320°). This points to the possibility that the simulated $m = 3$ traveling waves in the post-solstice period is closely related to the wave-form dust distribution while those in the pre-solstice period is largely driven by the energy conversion from the zonal flow. Note that the wave-form dust distribution also enhances the $m = 3$ waves in the pre-solstice period, but to a less degree (Fig. 17). For the post-solstice period, Fig. 18 also shows that the $m = 3$ forcing in Test 3 is stronger than that in Test 1. This may help explain the stronger $m = 3$ traveling waves in Test 3 despite of the similarity in the zonal mean structure near the surface between Test 3 and Test 1.

4.4. Additional sensitivity studies

To test which latitude band is more important, we have tried to reduce the latitudinal extent of the additional dust from 60° to 30° and prescribe it within 30–60°N, 45–75°N and 60–90°N with peak amplitude at 45°N, 60°N and 75°N, so that most of the prescribed dust resides outside, in the vicinity and inside of the polar vortex edge, respectively. The mean amplitudes of the eastward traveling $1.4 < T < 10$ sol $m = 3$ waves in the temperature field at $\sigma = 0.69$ are shown in Fig. 19. The left column is for traveling half sine wave dust blobs and the right column is for zonally uniform dust. All these simulations show a pre-solstice and a post-solstice maximum. It is interesting to notice that the 45–75°N simulations lead to the strongest $m = 3$ traveling waves that are about the same strength as those simulated in Test 1 (Fig. 17b), suggesting that dust storms within this latitudinal band are more efficient at enhancing these waves. The latitude versus height temperature structures of both the wave-form and zonally uniform 45–75°N simulations are almost the same as those for Test 1 as well (not shown). However, different from the conclusion drawn from Test 1 and Test 2 about the importance of wave-form dust distribution in the post-solstice period, the simulations here show little advantage of the wave-form over the uniform dust in terms of enhancing the post-solstice $m = 3$ traveling waves. This suggests that the wave-form dust storms with large latitudinal extent are probably better at enhancing the post-solstice $m = 3$ traveling waves. Flushing dust storms observed in images usually have large latitudinal extent stretching from the high to the low latitudes (Figs. 1 and 2). Further study is needed to illuminate the reason for the difference between the latitudinally extended and restricted dust storms.

We have also performed simulations where the three traveling dust concentrations reside within the 40–70°N latitudinal band and have narrower longitudinal half width (of 12.5° each) which implies weaker dust forcing at $m = 3$. We find that the simulated $m = 3$ traveling waves in temperature are about 20% stronger than those in the standard simulation, though they are weaker than those in Test 1. However, if we impose only one traveling dust concentration of the same shape as each individual used in Test 1, then the simulated $m = 3$ traveling waves have almost the same strength as that for the standard simulation. We find that the single traveling dust concentration does not change the zonal mean structure much and imposes little $m = 3$ wave-form forcing (not shown). The results presented in Section 4.1–4.3 suggest that large near surface baroclinicity and strong $m = 3$ dust forcing, probably among other unknown factors, are favorable for $m = 3$ traveling waves. These conditions are probably met more easily by coordinated traveling dust storms than by an isolated event.

We have experimented with different phases ($\varphi_0 = \pi/4, \pi/2, 3\pi/4$) for the traveling dust storms in Test 1 and found

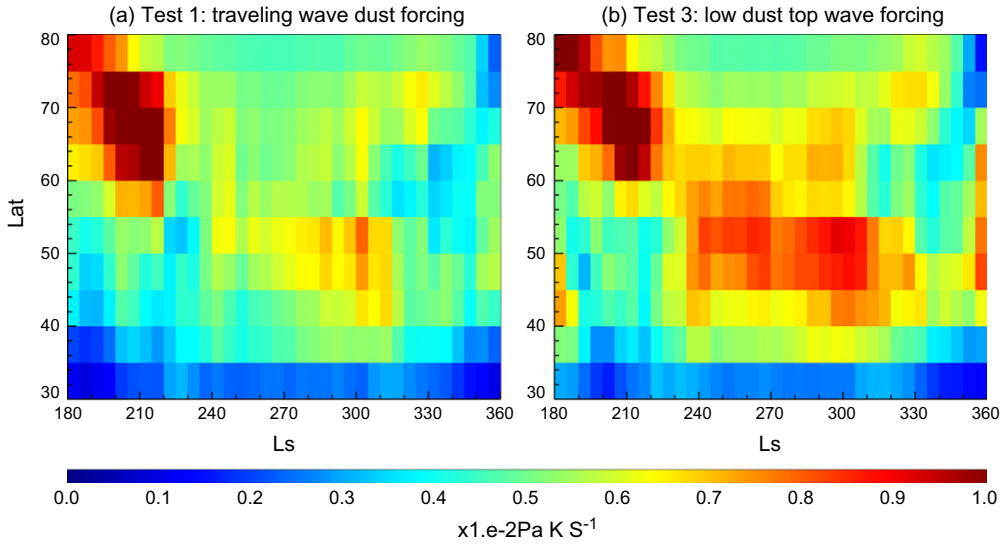

Fig. 18. The Ls versus latitude distributions of the mean amplitudes ($\times 10^{-2}$ Pa K S^{-1}) of the eastward traveling $1.4 < T < 10$ sol $m = 3$ waves derived from the net atmospheric heating rates at $\sigma = 0.69$ for (a) Test 1 and (b) Test 3.

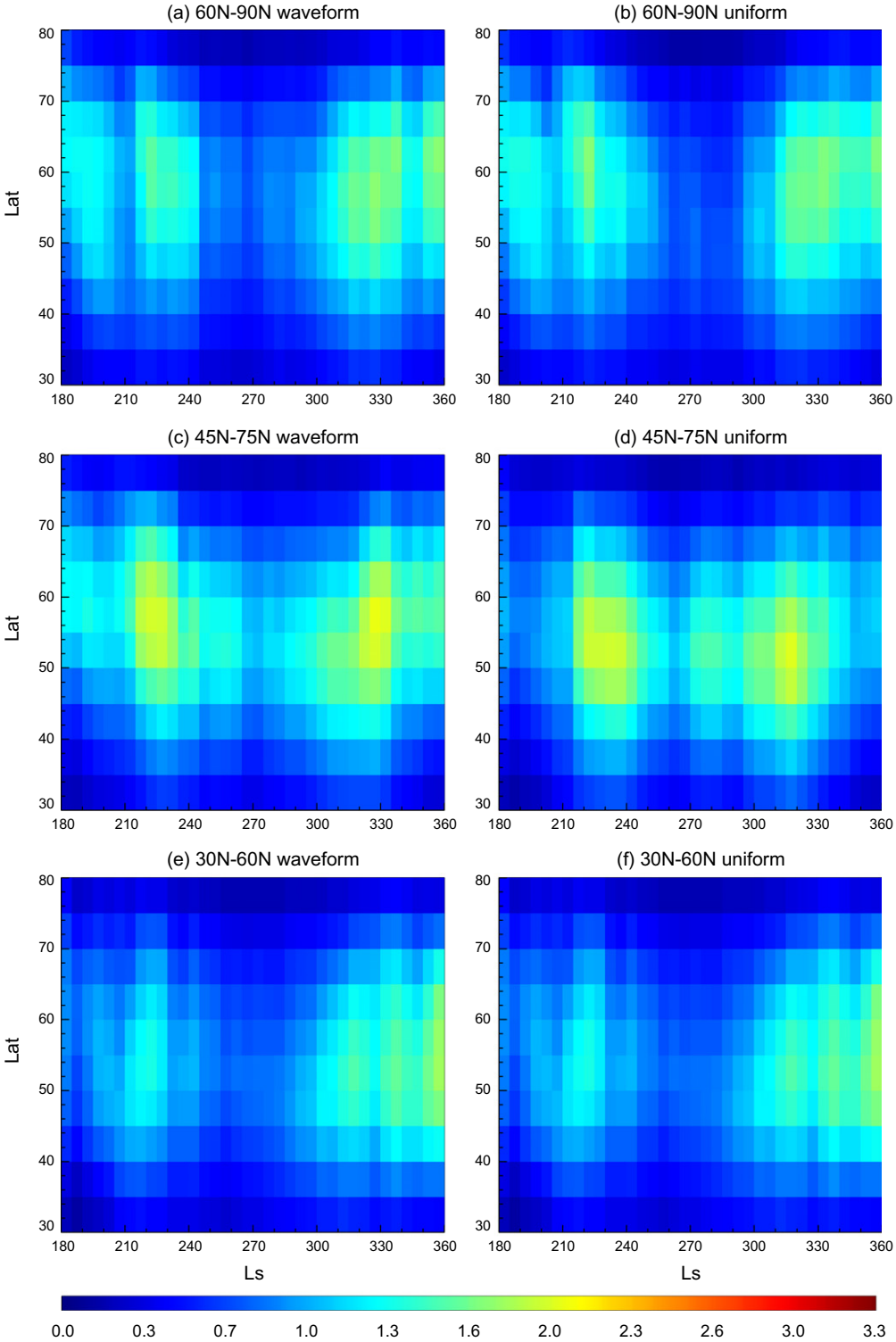

Fig. 19. The mean amplitudes of the eastward traveling $1.4 < T < 10$ sol $m = 3$ waves simulated by MarsWRF with (left column) wave-form and (right column) zonally uniform dust in addition to the "MGS dust scenario" within (top row) 60–90°N, (middle row) 45–75°N and (bottom row) 30–60°N.

no statistically significant difference with the results presented in Section 4.1. We have also plotted the simulated amplitudes of the $m = 3$ traveling waves as a function of their phases and have not found any particular relationship. These results suggest that the results in Section 1 are not sensitive to the phase of the forcing. Future work is needed for detailed investigation on the phase relationship.

In another experiment, we prescribed half the amount of dust in Test 1 (not shown). We find that the results in Section 4.1 are still qualitatively valid, though the simulated $m = 3$ traveling waves in near surface temperature are approximately 10–15% weaker than those in Test 1, but still significantly stronger than those in the standard simulation. In yet another simulation, we have deleted all the additional dust north of 60°N in Test 1, and find that there

is still significant $m = 3$ traveling wave enhancement with respect to the standard simulation, but the amplitude of the 90% percentile of the $m = 3$ traveling wave amplitude in near surface temperature is about 10% lower than that of Test 1.

We have conducted a MarsWRF simulation with the Mars Climate Database "Viking dust scenario" (Lewis et al., 1999) which has latitude-independent and time-dependent dust distribution that is about twice as dusty as the "MGS dust scenario". The simulated transient temperature variations (not shown) near the surface also exhibit a minimum during the winter solstice period, but the $m = 1$ and $m = 2$ traveling waves at $\sigma = 0.69$ are slightly weaker and the $m = 3$ traveling waves are stronger (approaching those in Test 2, the zonally uniform dust simulation) than those in the "MGS dust scenario" standard simulation. It is difficult to draw conclusions from a direct comparison between the "Viking dust scenario" and "MGS dust scenario" as the zonal mean temperature structure differs significantly over the planet.

5. Summary and discussion

This paper is motivated by the close correspondence between the curvilinear shaped traveling dust storms observed in images and the eastward traveling zonal wave number $m = 3$ waves derived from temperature data (Hinson and Wang, 2010; Hinson et al., 2012; Wang et al., 2005; Wang, 2007). We have performed MarsWRF GCM simulations to examine the seasonality, structure and dynamics of these waves and to test the hypothesis that the forcing associated with the traveling dust storms may enhance the $m = 3$ traveling waves, leading to a possible positive feedback.

We have used idealized dust distributions in this study. Specifically, we have used the "MGS dust scenario" for our standard simulation which serves as a baseline for comparison. It is a widely used dust scenario designed to represent a "typical" Mars year without the influence of any major dust storms. Moreover, it has been used in many previous studies with MarsWRF at a similar model resolution with overall satisfactory results (Richardson et al., 2007; Guo et al., 2009; Lee et al., 2009). Note that the results for other dust scenarios may differ from those for the "MGS dust scenario".

Our main test simulations employ three $T = 2.2$ sol eastward traveling dust blobs at northern mid/high latitudes during the fall and winter in addition to the "MGS dust scenario". The prescribed traveling dust blobs are meant to crudely represent at least a component of the dust distribution associated with the observed traveling dust storms in the vicinity of the polar vortex. The MOC and TES observations suggest that the curvilinear traveling dust storms are nicely correlated with the $m = 3$ traveling waves. Previous numerical studies suggest that dust can be arranged by the circulation to the corresponding traveling wave form (Wang et al., 2003, 2011; Basu et al., 2006). It should be noted that a MDGM usually shows only one or two traveling dust storms at the northern mid/high latitudes. However, since a MDGM is composed of 13 images taken from Sun-synchrous orbit during a sol, it is not an instantaneous camera shot. The possibility of three traveling dust storms cannot be ruled out.

The three traveling dust blobs introduce $m = 3$ Fourier mode in the dust distribution. Other zonal wave modes also exist due to the half-sine wave prescription, but their amplitudes are smaller. As the model simulates net heating when a dust blob is in the sunlight and cooling when it is in the dark (not shown), the wave spectra of the net radiative forcing due to the prescribed dust distribution are more complicated. We notice increased Fourier power at the zonal wavenumber and wave period of the prescribed dust storms, as well as large increase in various tidal modes in the net radiative forcing. This paper investigates only the collective effect due to the prescribed dust distribution. The effect due to different component of the radiative forcing requires further study.

We have prescribed traveling dust blobs throughout the northern fall and winter instead of just for the pre- and post-solstice periods when the observations show strong $m = 3$ traveling waves and active traveling dust storms. This provides us an opportunity to test the effect of this specific dust perturbation for the solstice period as well, had it existed. It does not mean to imply that traveling dust storms exist throughout the whole period.

The major traveling wave modes simulated by the standard simulation generally agree with those derived from the observations (Barnes, 1980; Banfield et al., 2004; Hinson, 2006) and simulated by other models (Barnes et al., 1993; Basu et al., 2006; Wilson et al., 2006). Similar to previous GCM studies (Basu et al., 2006; Wang et al., 2003; Wilson et al., 2006; Read et al., 2011; Wilson, 2011), our standard simulation also captures the observed seasonal pattern of stronger transient eddy temperature variations near the surface at northern mid and high latitudes before and after the winter solstice. The simulated meridional wind and eddy kinetic energy within the first scale height also exhibit this seasonality, but not the normalized surface pressure. The simulated $m = 1$ traveling waves have a large contribution to the surface pressure and a small contribution to the near surface meridional wind. The relative importance of the $m = 3$ traveling waves is greater in the near surface meridional wind than in the temperature. Using the GFDL Mars GCM, Basu et al. (2006) also found that the signature of $m = 3$ traveling waves was stronger in meridional wind than in temperature.

The simulated eastward propagating $1.4 < T < 10$ sol $m = 3$ waves are confined near the surface in terms of the temperature perturbation, EP flux and eddy available potential energy, but extend to higher altitudes in terms of the wind perturbations and eddy kinetic energy. This indicates a wave structure that is highly baroclinic near the surface and more barotropic above. Such a wave structure was previously simulated by Barnes et al. (1993) and is consistent with the MGS TES and Radio Science observations (Banfield et al., 2004; Hinson, 2006).

The simulated $m = 3$ traveling waves in the standard simulation are weaker than those observed. This result is obtained with the "MGS dust scenario" under a specific model setup. It does not mean to represent a general issue of the GCM. In this paper, we simply use the standard simulation as a reference to test if additional traveling dust blobs can enhance the simulated $m = 3$ traveling waves under the "MGS dust scenario" background. If true, then it implies that, at least under certain conditions, a positive feedback between the $m = 3$ traveling waves and the traveling dust storms is possible.

This study shows that the prescribed traveling dust blobs can enhance the simulated $m = 3$ traveling waves within the region and period where and when the observations show active traveling dust storms and strong $m = 3$ traveling waves. The presence of additional dust at northern mid/high latitudes (even without the $m = 3$ form) appears to be able to enhance the simulated $m = 3$ traveling waves over those in the standard simulation through changes in the zonal mean flow, especially for the pre-solstice period. The stronger $m = 3$ traveling waves in the test simulations correspond to a zonal mean structure that is characterized by more vertically oriented isotherms and a less pronounced near surface inversion at the northern mid/high latitudes during the relevant time periods. Such a zonal mean structure corresponds to a larger domain averaged baroclinic parameter in general, but the detailed relationship depends on how the baroclinic parameter is calculated. We have noticed that change in the zonal mean thermal structure is not the only factor. For dust blobs with large latitudinal extent, sufficient $m = 3$ radiative forcing due to traveling dust blobs also appears to be important, especially for the post-solstice

period. During the solstice period, the prescribed traveling dust blobs do not affect the simulated $m = 3$ traveling waves.

Comparing the results between Test 1 and Test 3, we find that the simulated $m = 3$ traveling waves are even stronger when dust blobs are concentrated near the surface. Comparing the results for dust blobs at different latitudes, we find that the 45–75°N band in the vicinity of the polar vortex is the most effective in terms of enhancing the simulated $m = 3$ traveling waves. We also find that a single traveling dust storm does not lead to enhancement of $m = 3$ traveling waves in the simulation, as it hardly influences the zonal mean thermal structure and leads to very little $m = 3$ radiative forcing.

The simulations in this study are useful for assessing the sensitivity of the major wave modes to perturbations in dust distribution. Based on our results, we suggest a possible positive feedback between coordinated traveling dust storms and $m = 3$ traveling waves when conditions are favorable. Further study is needed to better understand the conditions favorable for the $m = 3$ traveling waves. It should alto be recognized that we are not attempting to generate a completely realistic martian atmosphere on the basis of the prescribed dust distribution. It is clear that dust is a dynamic, interactive component of the martian atmosphere and that the complete effects of dust forcing require study using interactive dust (e.g. Newman et al., 2002; Basu et al., 2006; Kahre et al., 2006). We intend and hope that the results of the simplified simulations described in this paper will aid in the interpretation of the more complex, interactive dust simulations we envision for future work.

In this paper, we have investigated the effect of traveling dust storms on the traveling waves using MarsWRF. However, as shown in Fig. 1, there are abundant polar hood clouds as well as dust during the northern fall and winter. Using the MRO MCS data, Benson et al. (2011) showed that the north polar hood extended to the pole below about 40 km. These clouds may have important effect on the circulation, substantially increasing the strength of the baroclinic waves near the surface (Hollingsworth et al., 2011; Read et al., 2011; Wilson et al., 2007, 2011; Kahre et al., 2012). A useful next step would be to examine the influence of these clouds on the $m = 3$ traveling waves using idealized cloud forcing and to test their influence in isolation from and as an augmentation to the dust perturbations described here. Obviously, fully coupled interactive dust and ice simulations will be needed to completely simulate the processes in the system, probably best exploited with the use of data assimilation.

Acknowledgments

This paper is supported by the NASA Planetary Atmosphere program. The computations in this paper were run on the Odyssey cluster supported by the FAS Science Division Research Computing Group at Harvard University. Reviews by John Wilson and an anonymous reviewer have helped to improve this paper.

References

Andrews, D.G., Holton, J.R., Leovy, C.B., 1987. Middle Atmosphere Dynamics. The International Geophysics Series, vol. 40. Academic Press, San Diego.

Banfield, D., Conrath, B.J., Gierasch, P.J., Wilson, R.J., Smith, M.D., 2004. Traveling waves in the martian atmosphere from MGS TES Nadir data. Icarus 170, 365–403.

Barnes, J.R., 1980. Time spectral analysis of midlatitude disturbances in the martian atmosphere. J. Atmos. Sci. 27, 2002–2015.

Barnes, J.R., Pollack, J.B., Haberle, R.M., Leovy, C.B., Zurek, R.W., Lee, H., Schaeffer, J., 1993. Mars atmospheric dynamics as simulated by the NASA Ames general circulation model. 2. Transient baroclinic eddies. J. Geophys. Res. 98 (E2), 3125–3148.

Basu, S., Richardson, M.I., Wilson, R.J., 2004. Simulation of the martian dust cycle with the GFDL Mars GCM. J. Geophys. Res. 109, E11006. http://dx.doi.org/10.1029/2004JE002243.

Basu, S., Wilson, R.J., Richardson, M.I., Ingersoll, A.P., 2006. Simulation of spontaneous and variable global dust storms with the GFDL Mars GCM. J. Geophys. Res. 111, E09004. http://dx.doi.org/10.1029/2005JE002660.

Benson, J.L., Kass, D.M., Kleinbohl, A., 2011. Mars' north polar hood as observed by the Mars Climate Sounder. J. Geophys. Res. 116, E03008. http://dx.doi.org/10.1029/2010JE003693.

Briegleb, B.P., 1992. Delta-Eddington approximation for solar radiation in the NCAR community climate model. J. Geophys. Res. 97, 7603–7612.

Cantor, B.A., 2007. MOC observations of the 2001 Mars planet-encircling dust storm. Icarus 186, 60–96.

Collins, M., Lewis, S.R., Read, P.L., Hourdin, F., 1996. Baroclinic wave transitions in the martian atmosphere. Icarus 120 (2), 344–357. http://dx.doi.org/10.1006/icar.1996.0055.

Conrath, B.J., 1975. Themal structure of the martian atmosphere during the dissipation of the dust storm of 1971. Icarus 24, 36–46.

Conrath, B.J., Pearl, J.C., Smith, M.D., Maguire, W.C., Christensen, P.R., et al., 2000. Mars Global Surveyor Thermal Emission Spectrometer (TES) observations: atmospheric temperatures during aerobreaking and science phasing. J. Geophys. Res. 105, 9509–9519.

Dyer, A.J., Hicks, B.B., 1970. Flux-gradient relationships in the constant flux layer. Quart. J. Roy. Meteor. Soc. 96, 715–721.

Forget, F., Hourdin, F., Fournier, R., Hourdin, C., Talagrand, O., 1999. Improved general circulation models of the martian atmosphere from the surface to above 80 km. J. Geophys. Res. 104, 24155–24175.

Guo, X., Lawson, W.G., Richardson, M.I., Toigo, A.D., 2009. Fitting the Viking Lander surface pressure cycle with a Mars general circulation model. J. Geophys. Res. 114, E07006. http://dx.doi.org/10.1029/2008JE003302.

Haberle, R.M., Leovy, C.B., Pollack, J.B., 1982. Some effects of global dust storms on the atmospheric circulation of Mars. Icarus 50, 322–367.

Hinson, D.P., 2006. Radio occultation measurements of transient eddies in the northern hemisphere of Mars. J. Geophys. Res. 111 (E5), E05002, doi:10.1029/2005JE002612.

Hinson, D.P., Wang, H., 2010. Further observations of regional dust storms and baroclinic eddies in the northern hemisphere of Mars. Icarus 206 (1), 290–305. http://dx.doi.org/10.1016/j.icarus.2009.08.019.

Hinson, D.P., Wilson, R.J., 2004. Temperature inversions, thermal tides, and water ice clouds in the martian tropics. J. Geophys. Res. 109, E01002. http://dx.doi.org/10.1029/2003JE002129.

Hinson, D.P., Wang, H., Smith, M.D., 2012. A multi-year survey of dynamics near the surface in the northern hemisphere of Mars: Short-period baroclinic waves and dust storms. Icarus 219, 307–320.

Hollingsworth, J.L., Kahre, M.A., Haberle, R.M., Montmessin, F., 2011. Radiatively-active aerosols within Mars' atmosphere: Implications on the weather and climate as simulated by the NASA ARC Mars GCM. In: 4th International Workshop on the Mars Atmosphere: Modeling and Observations, Paris.

Hong, S.-Y., Noh, Y., Dudhia, J., 2006. A new vertical diffusion package with an explicit treatment of entrainment processes. Month. Weather Rev. 134, 2318–2341.

Hourdin, F., 1992. A new representation of the absorption by the CO_2 15-μm band for a martian general circulation model. J. Geophys. Res. 97, 18319–18335.

Kahre, M.A., Murphy, J.R., Haberle, R.M., 2006. Modeling the martian dust cycle and surface dust reservoirs with the NASA Ames general circulation model. J. Geophys. Res. 111, E06008. http://dx.doi.org/10.1029/2005JE002588.

Kahre, M.A., Hollingsworth, J.L., Haberle, R.M., 2012. Simulating Mars' Dust Cycle with a Mars General Circulation Model: Effects of Water Ice Cloud Formation on Dust Lifting Strength and Seasonality. Comparative Climatology of Terrestrial Planets, Lunar and Planetary Institute, Boulder, Colorado.

Lee, C., Lawson, W.G., Richardson, M.I., Heavens, N.G., Kleinbohl, A., et al., 2009. Thermal tides in the martian middle atmosphere as seen by the Mars Climate Sounder. J. Geophys. Res. 114, E03005. http://dx.doi.org/10.1029/2008JE003285.

Lee, C., Lawson, W.G., Richardson, M.I., Anderson, J.L., Collins, N., Hoar, T., Mischna, M., 2011. Demonstration of ensemble data assimilation for Mars using DART, MarsWRF, and radiance observations from MGS TES. J. Geophys. Res. 116, E11011. http://dx.doi.org/10.1029/2011JE003815.

Lewis, S.R., Collins, M., Read, P.L., 1999. A climate database for Mars. J. Geophys. Res. 104 (E10), 24,177–24,194.

Lewis, S.R., Montabone, L., Read, P.L., Rogberg, P., Wilson, R.J., Smith, M.D., 2008. Data assimilation of three Mars years of thermal emission spectrometer observations: Large-scale transient and stationary waves. In: Mars Atmosphere: Modeling and Observations Workshop, Williamsburg, VA.

López-Valverde, M.A., López-Puertas, M., 1994. A non-local thermodynamic equilibrium radiative transfer model for infrared emissions in the atmosphere of Mars 1. Theoretical basis and nighttime populations of vibrational levels. J. Geophys. Res. 99 (E6), 13093–13115, doi:10.1029/94JE00635.

McCleese, D.J., Heavens, N.G., Schofield, J.T., Abdou, W.A., Banfield, J.L., et al., 2010. Structure and dynamics of the martian lower and middle atmosphere as observed by the Mars Climate Sounder: Seasonal variations in zonal mean temperature, dust and water ice aerosols. J. Geophys. Res. 115, E12016. http://dx.doi.org/10.1029/2010JE003677.

Montmessin, F., Forget, F., Rannou, P., Cabane, M., Haberle, R.M., 2004. Origin and role of water ice clouds in the martian water cycle as inferred from a general circulation model. J. Geophys. Res. 109, E10004. http://dx.doi.org/10.1029/2004JE002284.

Newman, C.E., Lewis, S.R., Read, P.L., Forget, F., 2002. Modeling the martian dust cycle – 2. Multiannual radiatively active dust transport simulations. J. Geophys. Res. 107 (E12), 5124, doi:10.1029/2002JE001920.

Paulson, C.A., 1970. The mathematical representation of wind speed and temperature profiles in the unstable atmospheric surface layer. J. Appl. Meteor. 9, 857–861.

Read, P.L., Mulholland, D.P., Montabone, L., Lewis, S.R., 2011. Midwinter suppression of baroclinic strom activity on Mars: Observations and models. EPSC abstracts, 6, EPSC-DPS2011-1063, EPSC-DPS Joint Meeting 2011.

Richardson, M.I., Toigo, A.D., Newman, C.E., 2007. PlanetWRF: A general purpose, local to global numerical model for planetary atmospheric and climate dynamics. J. Geophy. Res. 112, E09001. http://dx.doi.org/10.1029/2006JE002825.

Smith, M.D., 2008. Spacecraft observations of the martian atmosphere. Annu. Rev. Earth Planet. Sci. 36, 191–219. http://dx.doi.org/10.1146/annurev.earth.36.031207.124335.

Strausberg, M.J., Wang, H., Richardson, M.I., Ewald, S.P., Toigo, A.D., 2005. Observations of the initiation and evolution of the 2001 Mars global dust storm. J. Geophys. Res. 110 (E2), E02006, doi:10.1029/2004JE002361.

Toigo, A.D., Lee, C., Newman, C.E., Richardson, M.I., 2012. The impact of resolution on the dynamics of the martian global atmosphere: Varying resolution studies with the MarsWRF. Icarus 221 (1), 276–288. http://dx.doi.org/10.1016/j.icarus.2012.07.020.

Ulbrich, U., Speth, P., 1991. The global energy cycle of stationary and transient atmospheric waves: Results from ECMWF analysis. Meteorol. Atmos. Phys. 45, 125–138.

Wang, H., 2007. Dust storms originating in the northern hemisphere during the third mapping year of Mars Global Surveyor. Icarus 189, 325–343. http://dx.doi.org/10.1016/j.icarus.2007.01.014.

Wang, H., Ingersoll, A.P., 2002. Martian clouds observed by Mars Global Surveyor Mars Orbiter Camera. J. Geophy. Res. 107 (E10), 5078, doi:10.1029/2001JE001815.

Wang, H., Richardson, M.I., Wilson, R.J., Ingersoll, A.P., Toigo, A.D., Zurek, R.W., 2003. Cyclones, tides, and the origin of a cross-equatorial dust storm on Mars. Geophys. Res. Lett. 30 (E9), 1488, doi:10.1029/2002GL016828.

Wang, H., Zurek, R.W., Richardson, M.I., 2005. The relationship between frontal dust storms and transient eddy activity in the northern hemisphere of Mars as observed by Mars Global Surveyor. J. Geophys. Res. 110 (E7), E07005, doi:10.1029/2005JE002423.

Wang, H., Toigo, A.D., Richardson, M.I., 2011. Curvilinear features in the southern hemisphere observed by Mars Global Surveyor Mars Orbiter Camera. Icarus 215, 242–252. http://dx.doi.org/10.1016/j.icarus.2011.06.029.

Webb, E.K., 1970. Profile relationships: The log-linear range, and extension to strong stability. Quart. J. Roy. Meteor. Soc. 96, 67–90.

Wilson, R.J., 2011. Dust cycle modeling with the GFDL Mars general circulation model. In: 4th International Workshop on the Mars Atmosphere: Modeling and Observations, Paris.

Wilson, R.J., Banfield, D., Conrath, B.J., Smith, M.D., 2002. Traveling waves in the northern hemisphere of Mars. Geophys. Res. Lett. 29 (14), 1684. http://dx.doi.org/10.1029/2002GL014866.

Wilson, R.J., Hinson, D., Smith, M.D., 2006. GCM simulations of transient eddies and frontal systems in the martian atmosphere. In: Second Workshop on Mars Atmosphere Modeling and Observations, Granada, Spain.

Wilson, R.J., Neumann, G.A., Smith, M.D., 2007. Diurnal variation and radiative influence of martian water ice clouds. GRL 34 (2), L02710. http://dx.doi.org/10.1029/2006GL027976.

Wilson, R.J., Lewis, S.R., Montabone, L., Smith, M.D., 2008. Influence of water ice clouds on martian tropical atmospheric temperatures. GRL 35 (7), L07202. http://dx.doi.org/10.1029/2007GL032405.

Wu, D.L., Hays, P.B., Skinner, W.R., 1995. A least squares method for spectral analysis of space-time series. J. Atmos. Sci. 52, 3501–3511.